The Meteoritical Society

Meteoritics & Planetary Science 1–23 (2019)
doi: 10.1111/maps.13265

Fine-grained material associated with a large sulfide returned from Comet 81P/Wild 2

Z. GAINSFORTH[1*], A. J. WESTPHAL[1], A. L. BUTTERWORTH[1], C. E. JILLY-REHAK[1], D. E. BROWNLEE[2], D. J. JOSWIAK[2], R. C. OGLIORE[3], M. E. ZOLENSKY[4], H. A. BECHTEL[5], D. S. EBEL[6], G. R. HUSS[7], S. A. SANDFORD[8], and A. J. WHITE[9]

[1]Space Sciences Laboratory, University of California, Berkeley, California 94720, USA
[2]Department of Astronomy, University of Washington, Seattle, Washington 98195, USA
[3]Department of Physics, Washington University in St. Louis, St. Louis, Missouri 63117, USA
[4]ARES, NASA Johnson Space Center, Houston, Texas 77058, USA
[5]Advanced Light Source, Lawrence Berkeley Laboratory, Berkeley, California 94720, USA
[6]Department of Earth and Planetary Sciences, American Museum Natural History, New York, New York 10024, USA
[7]University of Hawai'i at Manoa, Honolulu, Hawai'i 96822, USA
[8]NASA Ames Research Center, Moffett Field, California 94035, USA
[9]Department of Astrophysical and Planetary Sciences, University of Colorado, Boulder, Colorado 80309, USA
[*]Corresponding author. E-mail: zackg@ssl.berkeley.edu

(Received 25 April 2018; revision accepted 27 January 2019)

Abstract–In a consortium analysis of a large particle captured from the coma of comet 81P/Wild 2 by the Stardust spacecraft, we report the discovery of a field of fine-grained material (FGM) in contact with a large sulfide particle. The FGM was partially located in an embayment in the sulfide. As a consequence, some of the FGM appears to have been protected from damage during hypervelocity capture in aerogel. Some of the FGM particles are indistinguishable in their characteristics from common components of chondritic-porous interplanetary dust particles, including glass with embedded metals and sulfides and equilibrated aggregates. The sulfide exhibits surprising Ni-rich lamellae, which may indicate that this particle experienced a long-duration heating event after its formation but before incorporation into Wild 2.

INTRODUCTION

Anhydrous, fine-grained ("chondritic-porous") interplanetary dust particles (CP-IDPs) are regularly captured by aircraft-borne collectors in the stratosphere. Several lines of evidence point to a cometary origin for a subset of CP-IDPs (Love and Brownlee 1991; Brownlee et al. 1993; Joswiak et al. 2005), and while there is substantial evidence that some specific CP-IDPs are cometary (Joswiak et al. 2017), there is no definitive link between specific CP-IDPs and specific comets. CP-IDPs commonly contain 100–500 nm amorphous silicates known as GEMS (glass with embedded metals and sulfides), and crystalline silicate aggregates of similar and larger size called equilibrated aggregates (EAs). The relationship, if any, between GEMS and EAs is unclear, but a subset of EAs have compositions similar to GEMS and it has been suggested that many EAs are GEMS that have been heated and annealed (Brownlee et al. 2005; Keller and Messenger 2009). In addition to this fine-grained material (FGM), CP-IDPs also contain larger crystalline silicates; sulfides; and, more rarely, metal.

The Stardust mission returned ~300 μg of material from the coma of Jupiter-family comet Wild 2 to terrestrial laboratories, in a collector composed of aerogel and aluminum foil (Brownlee et al. 2006; Hörz et al. 2006; Brownlee 2014). There was an expectation that the Stardust collection would include abundant GEMS, EAs, and presolar grains. The collection was found to contain abundant crystalline particles $\gg 1$ μm in size (Brownlee et al. 2006), but evidence for GEMS and EAs has been elusive, probably because of the violence of the hypervelocity capture process and the fragility of FGM. Presolar grains have been reported, but the abundance is difficult to estimate accurately because of the uncertainties in survival efficiency (Floss et al. 2013).

Nevertheless, several particles extracted from the aerogel collectors have shown evidence for FGM adhering to their peripheries. These include Iris (C2052,12,74), a ≈15 μm chondrule-like object with associated primitive sulfides and an enstatite whisker (Stodolna et al. 2014), and Cecil (C2062,2,162), a particle containing a chondrule-like objects and fine-grained sulfides, spinels, and pyroxenes. In Cecil, the FGM was largely embedded in glass suggesting that some heating alteration may have occurred during aerogel capture, but several of the fine-grained components retained primitive signatures despite the apparent heating (Gainsforth et al. 2014b, 2015b). Joswiak et al. (2012) studied a sulfide particle, Febo (C2009,2,57), with FGM adhering to one side. This FGM showed strong evidence for melting, probably caused by aerogel capture. However, ^{15}N-rich organics survived in select locations within the FGM implying that at least some of the material in the Febo FGM retains chemical signatures from before aerogel capture (Matrajt et al. 2008).

Here we report the discovery and analysis of a particle named Andromeda (C2086,22,191) returned from comet 81P/Wild 2 by the Stardust spacecraft. It consists of a field of FGM in association with a large sulfide particle. Some FGM appears to have been protected from significant damage during hypervelocity capture in aerogel and has strong affinities with components of CP-IDPs, including GEMS and EAs.

METHODS

Andromeda is one of at least seven terminal particles of type-B (Burchell et al. 2008) track 191 (C2086,22,191, Figs. 1A and 1B). It was located at a depth of 8.8 mm from the space-exposed surface of the aerogel collector, and consisted of a 15 × 15 × 20 μm iron sulfide with abundant FGM aggregated in an embayment of the sulfide (Fig. 2). The particle was extracted in an aerogel "keystone" (Westphal et al. 2004), then embedded in EMBED 812 epoxy on the end of an epoxy bullet. We used an ultramicrotome to cut ≈100 nm thick sections, which we placed onto Cu TEM (transmission electron microscope) grids with a 10-nm amorphous carbon substrate (Ladd Research).

We studied Andromeda using an FEI Titan TEM operated at 80 and 200 keV at the Molecular Foundry, Lawrence Berkeley National Laboratory (LBL). A four-element Bruker silicon drift detector with a solid angle of 0.6 sr provided energy-dispersive X-ray spectroscopic (EDS) mapping in the Titan at count rates between 5 and 100 kcps. We used the Cliff–Lorimer approximation (Cliff and Lorimer 1975) with a thin film correction as described in Gainsforth (2016). Most spectra had on the order of 10^6 counts after background subtraction yielding detection limits <0.03 at % for most elements (Tables 1–4). In the case of the large sulfide given by spectrum Sulfide02 in Table 1 (abbreviated as: Table 1, Sulfide02), a longer spectrum of 3×10^8 counts allowed for quantification at hundreds of ppm concentration for several elements for which backgrounds were low. For sensitive phases that lose Na during TEM analysis, we acquired a sequence of EDS maps and then extrapolated the original Na content based on the observed loss rate which was found to be approximately linear for the beam dosages used. For the sulfide, the dose was sufficiently high that we applied a S volatilization correction (Gainsforth et al. 2014a). In many cases, it was not possible to fully remove the epoxy background from spectra and so we expect some O concentrations are a few percent too high. For quantification of Fe and O in iron oxides, the excess O from epoxy could have significantly altered the conclusions, so we subtracted a nearby epoxy spectrum by normalizing to Cl when possible, or C when the Cl signal was too weak.

We compared compositions of the FGM to solar system abundances from Lodders (2003). In most cases we chose to normalize against Mg rather than Si in order to avoid possible confusion with SiO_2 dilution from aerogel. To express elemental ratios with respect to protosolar values, we adopt the notation from astronomy:

$$[A/B]_{\odot} = \log_{10}\left(\frac{X_A/X_B}{(X_A/X_B)_{\odot}}\right) \quad (1)$$

where $\odot$ indicates the accepted protosolar values from Lodders (2003). Therefore, an A/B ratio which is exactly protosolar would mean $[A/B]_{\odot} = 0$, a 10× enhancement in A relative to B gives $[A/B]_{\odot} = 1$ and a 3× depletion in A relative to B gives $[A/B]_{\odot} = -0.5$. Within the uncertainties relevant to this paper, protosolar and CI abundances are equivalent with the exception of volatile elements such as O.

We carried out white-beam X-ray microdiffraction (μXRD) analyses on beamline 12.3.2 of the Advanced Light Source at LBL (Tamura et al. 2009). The μXRD beam was generated by a superconducting bend magnet and then collimated to a spot size of approximately 0.5 μm × 0.5 μm with Kirkpatrick–Baez mirrors and slits. We recorded the XRD patterns on a Dectris Pilatus 1M camera. By acquiring 2D spatial maps with a diffraction pattern at each position, we were able to analyze the

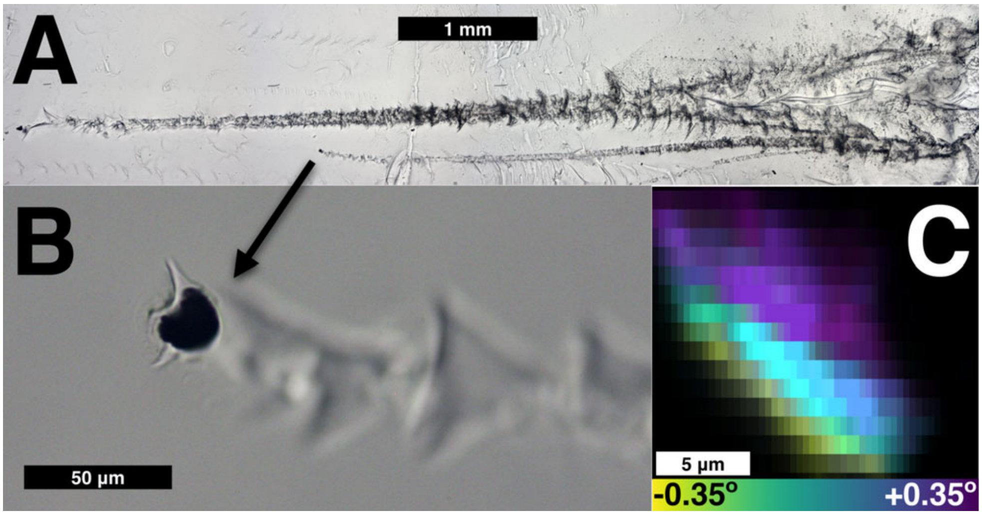

Fig. 1. A) Optical mosaic image of track 191 produced from image stacks at varying focus. Andromeda was found at the end of an 8.8 mm track. The arrow connects the location of Andromeda in the track to panel (B). B) Optical zoom-in of Andromeda. C) XRD topograph of Andromeda showing that the sulfide is a single crystal but with three subgrains spaced in 0.35° increments. Due to sample preparation and beamline geometry, panel (C) is not at the same viewing angle as panels (A) and (B).

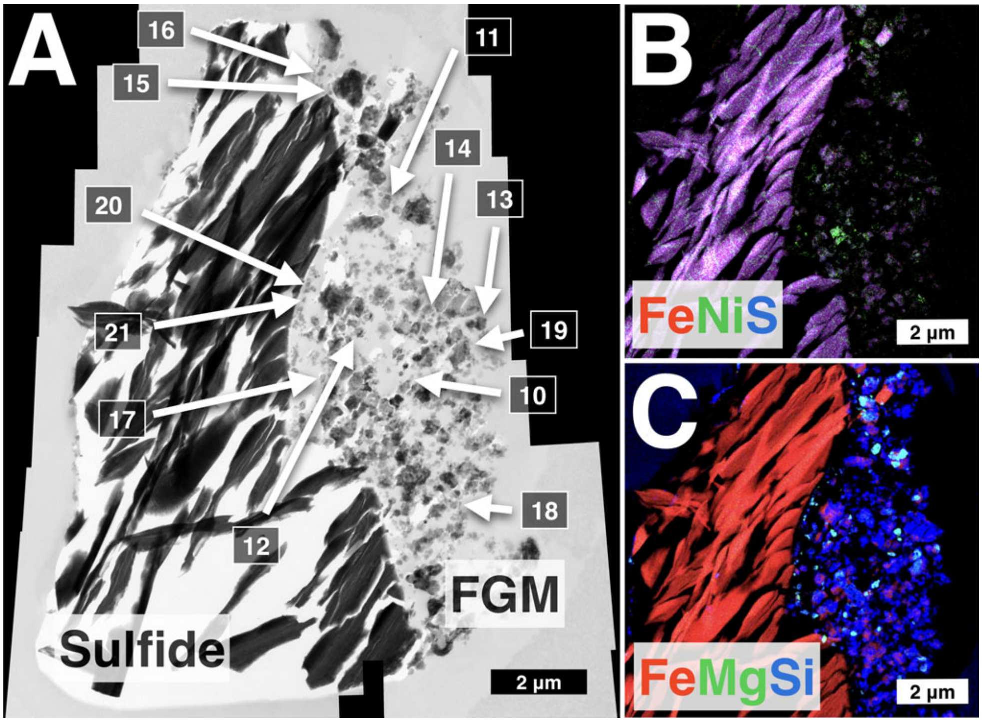

Fig. 2. A) Mosaic of bright field TEM images of Andromeda showing the sulfide on the left, and fine-grained material (FGM) on the right. Objects in the FGM are labelled according to their names in Table 2. B) EDS map of the FGM with iron (red), nickel (green), and sulfur (blue). The Ni content in the FGM is significantly higher than the Ni content of the primary sulfide impactor. C) EDS map of the FGM with iron (red), magnesium (green), and silicon (blue). Mg-rich grains include equilibrated aggregates, GEMS and altered objects. The interstitial space is filled with epoxy.

crystal distortion as a function of its position. By tracking the presence and location of a single diffracted beam in each of the diffraction patterns, we were able to produce topographs: images of the crystal locations and distortions much like dark-field electron microscopy does in a TEM. For details on the method in general,

Table 1. Sulfide compositions from TEM EDS (atomic %).

	Atomic %			ppm								
Spectrum	S	Fe	Ni	Cr	Mn	Se	$\frac{\Sigma\text{Cations}}{(\text{S}+\text{Se})}$	τ[a] (nm g cm^{-3})	Diffraction	$[\text{Ni/Fe}]_{\odot}$[b]	$[\text{S/Se}]_{\odot}$[b]	Notes
Andromeda:												
Sulfide01	49.86	49.99	0.15				1.01	0		−1.3		Cliff–Lorimer
Sulfide02	49.99	49.87	0.10	350		70	1.00	279		−1.5	0.02	High-counts
Sulfide03	49.95	49.93	0.13				1.00	358	Troilite[c]	−1.3		Fe matrix
Sulfide04	50.00	49.52	0.48				1.00	358	Pyrrhotite[c]	−0.8		Ni band
Sulfide05	49.78	49.25	0.97				1.01	358		−0.5		Highest Ni
Sulfide06	53.35	39.73	6.93				0.88	n/a				Calculated[d]
Sulfide07	47.14	52.12	0.60				1.12	300		−0.7		P detected
Febo:												
Sulfide08	53.34	45.76	0.79	280	620	160	0.87	450	nC	−0.5	−0.3	

[a] Mass thickness of sample used for thin film EDS correction.
[b] Ratio normalized to solar system abundances, see text.
[c] The thickness correction has been chosen to optimize for troilite.
[d] This idealized composition of the pyrrhotite bands was calculated in the discussion by combining HRTEM, diffraction, and EDS.

see Black and Long (2004), and for details on our specific implementation, see Tamura (2014) and Gainsforth et al. (2013a).

For estimation of gas temperatures during capture in aerogel, we computed dissociation energies for aerogel and troilite into gases using density functional theory (DFT) implemented in the plane wave formalism as part of the Quantum Espresso suite (Giannozzi et al. 2009). We used Perdew–Burke–Ernzerhof pseudopotentials from the Standard Solid State Pseudopotentials Efficiency database (Vanderbilt 1990; Perdew et al. 1996; Corso 2014). We used single-unit-cell quartz and troilite structures for solid SiO_2 and FeS, and a 5 Å cubic volume for molecules. Quartz was chosen as a proxy for aerogel since the two are expected to have formation energies within a few hundred meV of each other based on examination of SiO_2 structures in the Materials Project (Jain et al. 2013), and examination of thermodynamic constants from the NIST-JANAF thermodynamic tables (Chase 1998). Convergence criteria were set to $\Delta E \leq 40$ meV in accordance with the expected accuracy of the pseudopotentials (Lejaeghere et al. 2016). Computation was done on the Vulcan, Nano, and Etna compute clusters at LBL.

RESULTS

Large Sulfide

μXRD analysis showed that the sulfide was a polygonalized crystal, consisting of three domains rotated by 0.35° from each other. Figure 1C shows a topograph produced from a Laue map that shows the location and size of each domain. The reflections seen in XRD show multiple maxima within each reflection (expected for polygonalized crystals) and also show broadening of the peaks that indicate large internal stresses on the scale of 1° over the entire width of the crystal. The diffraction pattern fits pyrrhotite 4C. Because the internal strains are so large, it is not possible to differentiate troilite from pyrrhotite on the basis of the unit cell shape.

The (Fe+Ni)/S ratio measured by TEM/EDS was 1.01:1, as expected for troilite, not pyrrhotite 4C (Table 1). Ni was partitioned out of the sulfide with respect to Fe: $[\text{Ni/Fe}]_{\odot} < -1$. Such Ni partitioning is also seen in several other Stardust sulfides (Joswiak et al. 2012; Gainsforth et al. 2013b). $[\text{S/Se}]_{\odot} = 0.02$, indicating no significant fractionation of selenium from the protosolar abundance ($\text{S/Se} = 6.8 \cdot 10^3$). High-resolution EDS maps showed that Ni is concentrated in bands no more than a few tens of nm thick rather than homogeneously distributed throughout the sulfide (Fig. 3A). The observed variability of Ni-rich band widths may be consistent with varying viewing angles of thin (≤30 nm) lamellae within the Ni-poor sulfide matrix. The average of three linescans across different Ni-rich bands is shown in Fig. 4 as the difference in composition from ideal troilite. Ni and Fe are anti-correlated in the Ni-rich region. S appears to increase in the Ni-rich bands, but the deviation is no more than the deviation in S content outside the Ni-rich region and could be systematic error due to variable thickness of the sulfide. The linescan is limited by the spatial resolution of the EDS map at ≈30 nm.

Selected area electron diffraction (SAED) showed that the structure is best described by a superposition of troilite (zone [110]) and pyrrhotite 4C (zone [100]), though the pyrrhotite superlattice reflections are weak in comparison with those of the troilite (Fig. 3C). High-resolution transmission electron microscopy (HRTEM)

Table 2. Nanophase object compositions from TEM EDS (atomic %).

	Atomic %																
#	O	Na	Mg	Al	Si	P	S	K	Ca	Ti	Cr	Mn	Fe	Ni	τ	O/Si	(Mg+Al+ Ca+Fe)/Si	Notes
FGM09	52.92	0.27	1.33	0.25	17.39	0.17	11.60	0.13	0.57	b.d.	0.04	0.03	15.17	0.14	300	3.04	1.00	FGM bulk
FGM10	61.29	0.12	10.86	1.20	17.03	0.10	3.47	0.16	0.49	0.03	0.14	0.06	4.82	0.23	300	3.60	1.02	
FGM11	64.49	0.41	13.77	1.15	14.76	0.15	0.37	0.19	0.49	0.03	0.16	0.15	3.73	0.15	300	4.37	1.30	
FGM12	59.59	0.32	16.91	1.20	16.31	0.20	0.46	0.17	0.22	0.03	1.13	0.15	3.29	0.03	300	3.65	1.33	
FGM13	43.52	0.04	4.24	0.72	13.98	b.d.	17.51	0.09	0.37	0.09	0.06	19.11	0.25	0.03	300	3.11	0.40	Zn det.
FGM14	66.17	0.80	14.70	1.19	12.73	0.22	0.93	0.07	0.26	0.05	0.09	b.d.	2.55	0.19	300	5.20	1.47	
FGM15	62.90	b.d.	12.41	0.93	12.95	0.12	0.80	0.07	0.58	0.04	0.21	0.09	8.62	0.29	300	4.86	1.74	
FGM16	60.55	0.38	9.04	1.27	16.14	0.12	2.68	0.10	1.31	0.02	0.16	0.11	7.93	0.22	300	3.75	1.21	Has Fe oxides
FGM17	62.16	0.19	10.74	0.77	14.48	0.44	0.73	0.12	0.86	0.01	0.42	0.10	8.95	0.02	300	4.29	1.47	Has Fe oxides
FGM18	62.37	0.27	6.29	1.31	18.10	0.08	1.46	0.14	1.72	0.03	0.12	0.04	7.74	0.34	300	3.45	0.94	
FGM19	57.64	0.14	3.56	0.27	20.31	0.039	7.65	0.03	0.21	b.d.	0.04	0.06	9.90	0.15	300	2.84	0.69	
FGM20	65.24	0.41	9.51	0.89	13.42	0.25	1.07	0.21	0.94	0.02	0.15	b.d.	7.81	0.06	300	4.86	1.43	Zn det., has Fe oxides
FGM21	58.75	0.07	2.60	1.62	21.53	0.30	1.33	0.38	0.38	0.06	0.32	b.d.	12.08	0.61	300	2.73	0.77	

Atomic ratios normalized to protosolar and Mg are in Table S1 in supporting information.

Table 3. Fe Oxide compositions from TEM EDS (atomic %).

	Atomic %														
#	O	Na	Mg	Al	Si	P	S	K	Ca	Fe		τ	O/Fe	Background[a]	Notes
FeOx22	65.65	b.d.	b.d.	0.15	0.68	det.	1.64	b.d.	0.34	31.49	0.06	300	2.08	Cl	Near FGM16
FeOx23	50.89	b.d.	b.d.	b.d.	2.33	0.49	1.28	b.d.	0.58	44.44	b.d.	300	1.15	Cl	Near FGM16
FeOx24	63.88	b.d.	b.d.	b.d.	4.29	0.69	2.23	b.d.	0.63	28.28	b.d.	300	2.26	C	Near FGM16
FeOx25	59.70	b.d.	b.d.	b.d.	0.96	0.37	1.10	b.d.	0.47	37.40	b.d.	300	1.60	Cl	Near FGM16
FeOx26	56.70	b.d.	0.61	b.d.	2.42	0.37	1.47	b.d.	0.43	38.00	b.d.	300	1.49	Cl	Near FGM16
FeOx27	63.52	0.93	0.60	b.d.	1.38	0.50	1.89	0.32	1.95	28.92	b.d.	300	2.20	C	Near FGM17
FeOx28	59.40	1.46	b.d.	b.d.	1.67	0.96	2.60	0.68	2.16	31.07	b.d.	300	1.91	C	Near FGM17
FeOx29	53.11	b.d.	0.41	0.18	b.d.	0.20	0.69	b.d.	b.d.	44.53	0.83	300	1.19	Cl	Lambda magnetite. Cr det.

[a] Element for normalizing and subtracting the background. See Methods section.

Table 4. Pyroxene compositions from TEM EDS.

	Normalized oxide weight %										
Spectrum	SiO_2	TiO_2	Al_2O_3	Cr_2O_3	MgO	CaO	FeO	Na_2O	P_2O_5	S	Phase[a]
Px30	56.14	0.25	0.95	4.23	14.81	16.26	3.94	2.28	1.00	0.14	$En_{40}Fs_{07}Wo_{33}Ko_{14}Ja_{06}$

	Cations per 6 oxygens											
Spectrum	Si	Ti	Al	Cr	Mg	Ca	Fe	Na	P	S	ΣCations	τ[b]
Px30	2.02	0.01	0.04	0.12	0.80	0.63	0.12	0.16	0.03	0.01	3.90	300

[a] En = enstatite; Fs = ferrosilite; Wo = wollastonite; Ko = kosmochlor; Ja = jadeite.
[b] $nm \cdot g\ cm^{-3}$.

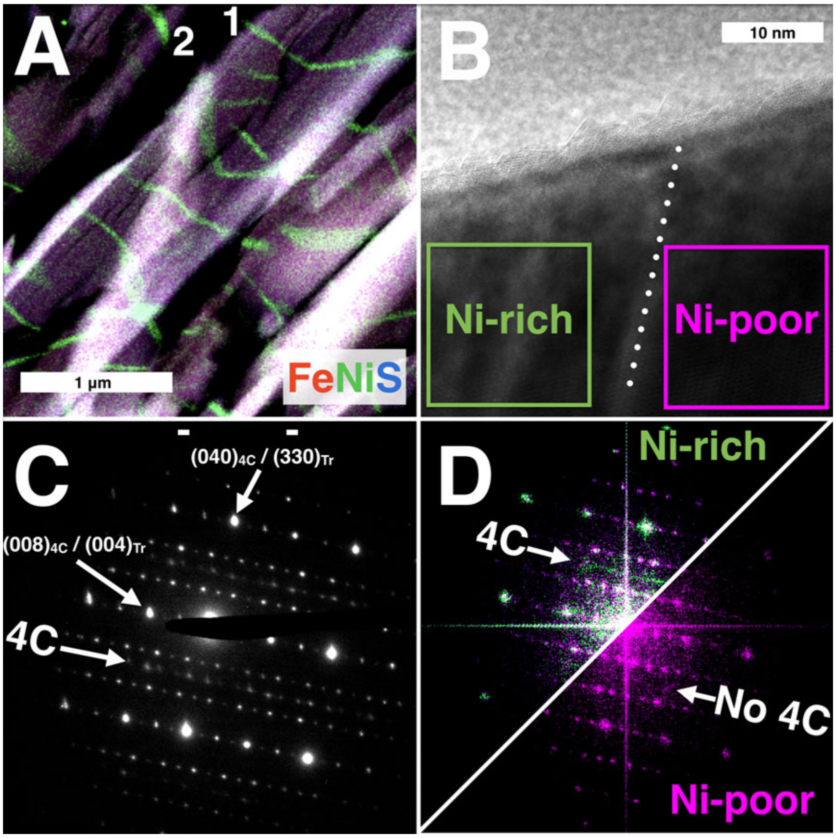

Fig. 3. A) EDS map showing troilite (purple) with Ni-rich bands (green). B) HRTEM image down the [110] troilite axis with a Ni-rich band on the left and a Ni-poor region on the right. The boxes show the regions used to produce FFTs of each region (shown in [D]). C) SAED of region including Ni-rich and poor regions down the [110] (troilite) or [100] (pyrrhotite 4C) zone axis. Pyrrhotite 4C superlattice reflections (4C) are marked alongside troilite (Tr). D) HRTEM FFT shows the same pattern. Purple spots are from the FFT of the Ni-poor region (box shown in [B]) and green shows the FFT from the Ni-rich region (box shown in [B]). The Ni-rich FFT shows the pyrrhotite 4C superlattice reflections.

of the Ni-rich bands down the [110] zone axis of troilite show that they exhibit the pyrrhotite 4C superlattice reflection, and the Ni-poor regions do not (Fig. 3D). We measured the broadening of the (11n) family of superlattice reflections after subtracting the instrumental response (22n) using the method of Gainsforth et al. (2017b) and we found the spread to be 0.28 nm^{-1} in the c* direction.

Fine-Grained Material

Andromeda contained a field of FGM, partially embayed in the large sulfide, with ≈50 Mg-rich particles in the ultramicrotomed section shown in Fig. 2. We estimate that several hundred such particles were probably present in total, considering that the microtomed section is only a 100- to 200-nm-thick sampling of a 3D

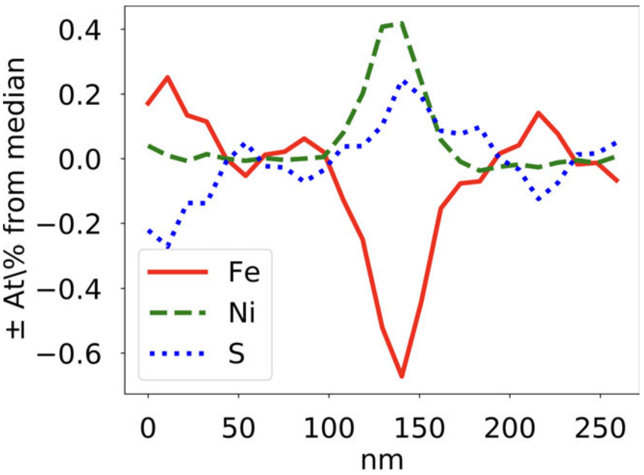

Fig. 4. Average of three linescans across Ni-rich bands. The Ni content is higher and the Fe content lower in the Ni-rich bands. The variability of S across bands is not clear.

volume. TEM and scanning transmission X-ray microscopy (STXM) analysis showed that the embedding epoxy penetrated the interstial spaces in the FGM during sample preparation, indicating that the material was porous prior to embedding.

When normalized to Si and protosolar ratios, we find that the FGM is depleted in Na, Mg, Al, Ca, Cr, Mn, and Ni, and enriched in P, S, Fe, and K (Table 2, FGM09). K was present at ≈2 times protosolar abundance, normalized to Si, but no K-rich minerals were observed.

We studied five classes of particles in the FGM field, discussed in detail below: GEMS-like objects, EA-like objects, Fe oxides, kosmochloric pyroxene, and sulfides.

GEMS-Like Objects

The mean composition of GEMS differs from that of the solar system (Keller and Messenger 2011). Keller and Messenger (2011) and Messenger et al. (2015) measured compositions of 287 GEMS, from which we calculated mean compositions and standard deviations for each element. We used a χ^2 test to determine if objects within the FGM were consistent in their elemental composition with GEMS:

$$\chi^2 = \sum_{\text{elements}} \frac{(X - \bar{X}_{\text{GEMS}})^2}{\sigma^2_{\text{GEMS}}} \tag{2}$$

where X is the atomic fraction of an element in the particle, $\bar{X}_{\text{GEMS}}$ and σ_{GEMS} are the mean and standard deviation, respectively, of the atomic elemental fractions, measured in a large number of GEMS from Keller and Messenger (2011) and Messenger et al. (2015). To compute χ^2, we used atomic fractions of eight elements and report the reduced χ^2 (χ^2_ν, $\nu = 7$ degrees of freedom) along with p, the probability that the composition is inconsistent with that of the GEMS distribution. Since low-Z elements are susceptible to significant instrumental differences and are often more volatile, we have not included elements with Z ≤ Na in the computation of χ^2. For the purpose of computing p, we made the simplifying assumption that the elemental abundances are normally distributed independent variables (e.g., we ignored the correlation between Fe and S). This assumption is conservative in the sense that it tends to overestimate p.

We acquired quality EDS maps and images of about 10 objects within the FGM that have compositions vaguely reminiscent of GEMS. The compositions of each is listed in Table 2. We ultimately studied each nanophase object using a full spectrum of TEM techniques including EDS maps to obtain compositional information, as well as imaging and diffraction to obtain petrographic information. However, to estimate bias in our choice of objects, we observed that GEMS and some EAs have compositions similar to each other and distinct from other materials. We used k-means clustering (Arthur and Vassilvitskii 2007) on the EDS map from Fig. 2 to identify 52 regions which could be GEMS-like, so we studied $\sim 20\%$ of the potential GEMS-like objects in this field, based on composition alone.

We observed an object (FGM10) which had the appearance and composition of a GEMS (Fig. 5; Table 2, FGM10, $p = 0.2$). The top and left edges were bounded by ≈100 nm euhedral sulfides. The core contained Fe-Ni metal inclusions 5–20 nm in size. Within the metal inclusions, $[\text{Ni/Fe}]_\odot$ was ≈ 0.3, while the external sulfide had $[\text{Ni/Fe}]_\odot \approx 0.0$. EDS maps show zoning of Mg and Ca within the core, a feature that has been noted within GEMS in IDPs (Joswiak et al. 1996; Keller and Messenger 2011). The sulfide on the lower right was more rounded and some sulfur was present in the nearby silicate portion, penetrating approximately half of the silicate. One metal-core/sulfide-shell structure was present in the silicate region containing the diffuse S.

EA-Like Objects

Two objects in the FGM field showed morphologies reminiscent of equilibrated aggregates in CP-IDPs. FGM11 (Fig. 6) contained Mg-rich ≈ 10 nm silicate crystals. The silicate crystals showed mosaicity; that is, they were oriented within a few degrees of each other. It also contained Fe-Ni metals, sulfides, Cr-rich hotspots (probably chromite), and Al-rich inclusions. The outline of the object was defined by the euhedral edges of the silicate crystals. There was no attached silica melt, anhedral sulfide, or any other phase to indicate alteration during capture.

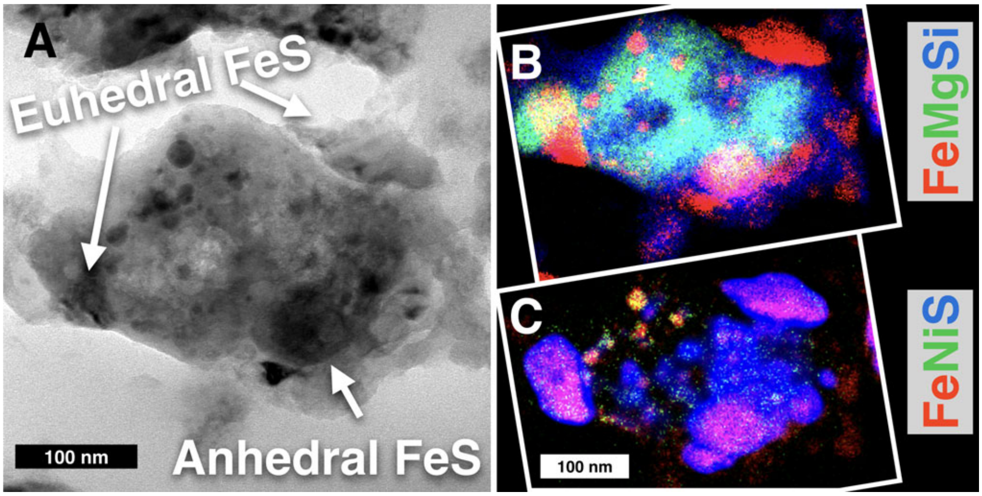

Fig. 5. A) BF TEM image of FGM10, a GEMS-like object in Andromeda's FGM. Euhedral sulfides are present on one side of the object. B) EDS map showing Fe (red), Mg (green), Si (blue). Mg shows distinct inhomogeneity. C) EDS map showing Fe (red), Ni (green), S (blue, with a three pixel gaussian filter). Fe-Ni metals are present within the body of the object.

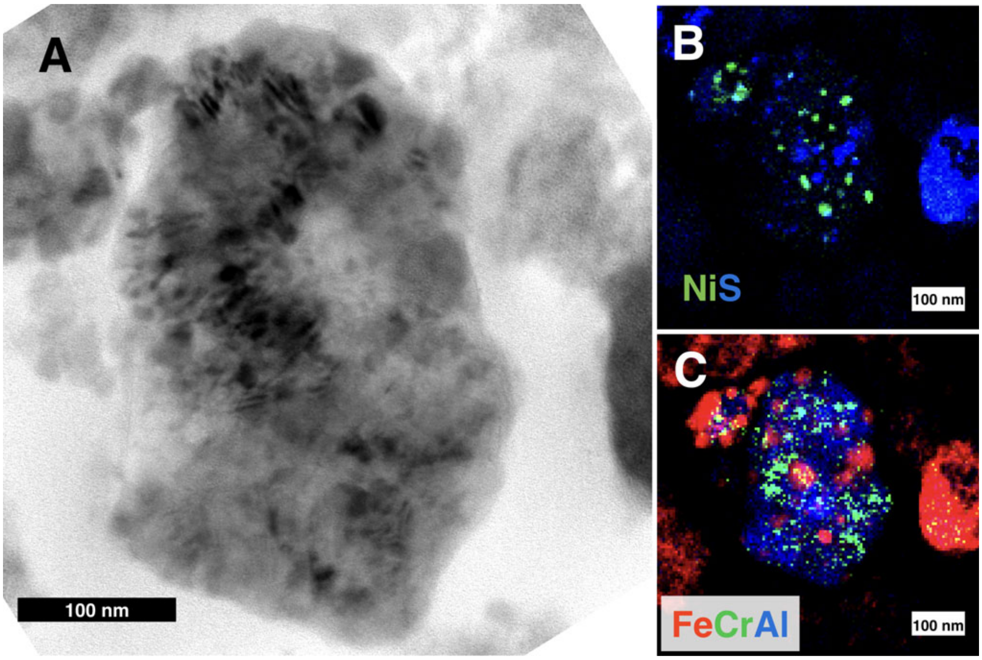

Fig. 6. A) BF TEM image of FGM11, an equilibrated aggregate (EA) in Andromeda's FGM. B) EDS map of EA showing the location of Ni-rich metals (green) and the presence of sulfides (blue). C) EDS map of EA showing the location of Cr-rich inclusions (green) and an Al-rich inclusion and surrounding Al-rich silicates (blue).

FGM12 was a second particle with an equilibrated aggregate morphology and contained Mg-rich silicate crystals. There were several Fe-Ni metal and sulfide inclusions, and no core-rim structures. The periphery was surrounded by euhedral chromite crystals, and was well defined by their shapes (see Fig. S1 in supporting information).

Heated GEMS-Like and EA-Like Objects

Additional objects were present that had characteristics of GEMS or EAs, but showed indications of significant heating.

FGM13 is morphologically reminiscent of GEMS but is compositionally inconsistent with GEMS

($p > 0.99$) because of a large excess of sulfide and Cr relative to the other elements. In the core are Fe-Ni metal inclusions with $[\mathrm{Ni/Fe}]_{\odot} = -0.04$. There was one euhedral sulfide on the left face with $[\mathrm{Ni/Fe}]_{\odot} = -0.55$. The remaining sulfide resided around the periphery, was morphologically nebulous, and conformally coated the object. A metal-core/sulfide-rim structure was visible in the silicate portion of the object.

FGM14, FGM15, and FGM16 were all spherical objects 100–200 nm across with $p = 0.5$–0.8. The bulk of the material was silicate with crystalline domains, though possibly amorphous silicate was present as well. In and around the silicate were Fe-Ni metals and sulfides. They did not contain euhedral sulfides around the periphery, with the possible exception of one sulfide adjacent to FGM14. They did not show evidence for the core-rim structures caused by aerogel capture, and they did not show evidence for excess SiO_2. Figure S2 in supporting information shows an HRTEM and digital darkfield image of FGM15 showing the near-perfect spherical shape and the presence of crystalline domains. FGM16 (Fig. 7) was apparently sintered to amorphous Fe oxide. Additional Fe oxides containing Mg, Al, Si, P, S, Ca, and Ni were present in the vicinity. These oxides are described in the next section and are a primary reason for considering these to be heated.

FGM17 contained crystalline Mg-rich silicates exhibiting triple junctions and chromite inclusions as shown in Fig. S3 in supporting information. It is associated with an Fe oxide similar to the oxide adjacent to FGM16. Fe was also visible as a web-like structure weaving around the periphery of the object and outlining the crystals. There are no core-rim structures or excess silica.

FGM18 was reminiscent of GEMS but contained a metal-core/sulfide-rim structure. There were no euhedral crystals around the periphery: instead, all crystals within and without were rounded. There was no evidence of crystalline silicate, but the Mg formed a web-like structure throughout the object interconnecting the Fe-Ni metals. The outer periphery of the object was rich in Ca (see Fig. S4 in supporting information).

FGM19 was similar to common aerogel capture products seen by Ishii et al. (2008) (Fig. 8). It contained multiple metal-core/sulfide-rim structures. We observed vesicular structures and substantial excess silica. The periphery was lined by amorphous web-like FeS.

FGM20 was located at the boundary between the sulfide and FGM, touching the sulfide, and contained amorphous and poorly crystalline objects. The outlines of Al-rich silicate, Ca-rich silicate, and Mg-rich silicate could be seen but were not crystalline. An amorphous silicate with Fe-Ni metal grains and Fe-Ni-S grains was attached to one side. Several small beam-sensitive, amorphous Fe oxides were present around the periphery (see Fig. S5 in supporting information).

FGM21 was also located at the sulfide/FGM boundary and contained the highest K and P

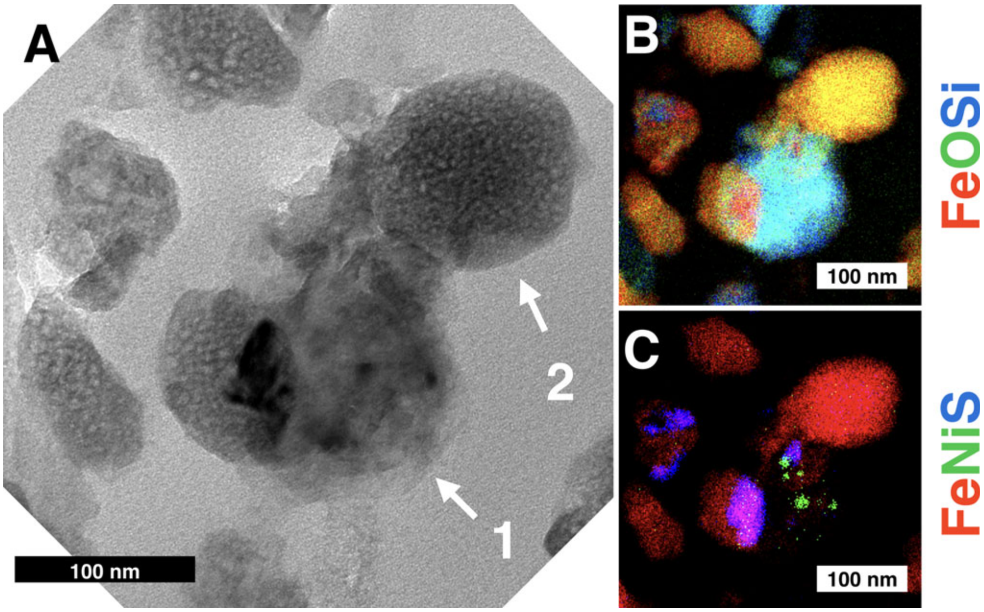

Fig. 7. A) BF image of FGM16. The location marked (1) is the equilibrated aggregate. (2) is one of several Fe oxides. B) EDS map showing the Si-rich aggregate (cyan) contrasted with the Fe oxides (yellow). C) EDS map showing the presence of Ni-rich metals inside the equilibrated aggregate (green), the Fe oxides (red), and sulfides (purple).

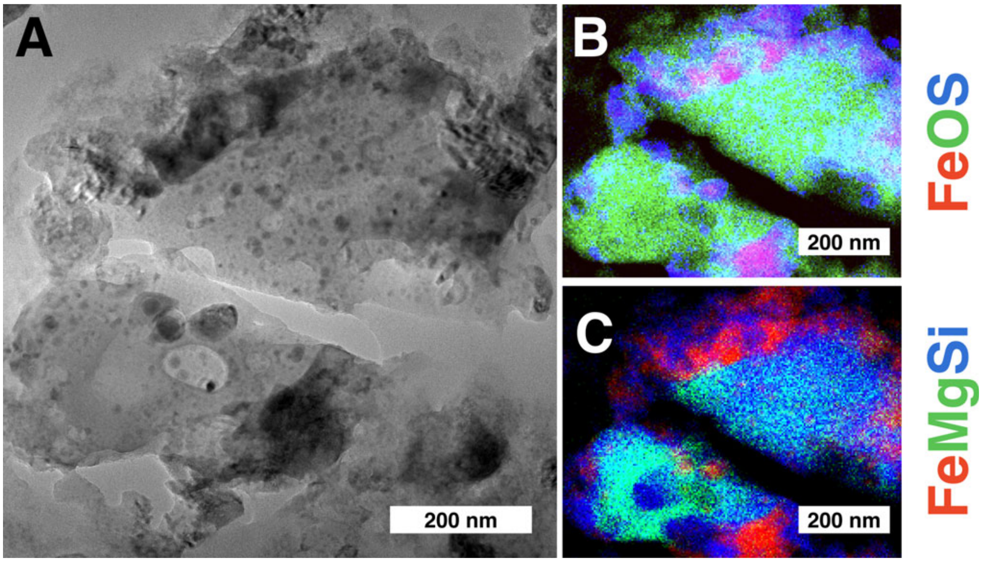

Fig. 8. A) BF image of FGM19. Vesiculated structure and Fe-core/sulfide-rim structures are visible. The periphery was surrounded by sulfides. The object is bisected by ultramicrotomy. B) EDS map showing Fe-cores (red) and sulfide rims (blue). The periphery also contains sulfides, which have a web-like texture from volatilization during aerogel capture. C) EDS map showing vesicles in the silicate where Mg (green) is absent.

concentration of any particle we measured. The P was largely concentrated into a ≈ 10 nm diameter Fe-Ni-P hotspot that could have been schreibersite, and appeared to have a core-shell structure in HAADF. Fe-Ni metals were also present, sulfur was diffused throughout the silicate, and no sulfides were visible. The Mg and Al were present near the center but segregated from each other, and a 5-nm Ti hot spot was present in the Al-rich portion of the EDS map.

Iron Oxides in FGM

Diffraction analyses of the Fe oxides near FGM16 showed that they were amorphous. Comparison of HAADF images taken before and after EDS mapping of the oxides around FGM20 showed that the Fe oxides were beam sensitive.

The Fe oxides were most prevalent at the interface between the FGM and the sulfide, and in the large voids between clumps of material within the FGM. The oxides were also present on the leading edge of the sulfide away from the FGM. They were not frequently found within clumps of FGM material.

For comparison, we examined a magnetite rim from a lightly heated CP-IDP (Lambda, Cluster IDP L2071,17). The bright field image shown in Fig. 9A shows that the rim was nanocrystalline, although it may also have included some amorphous regions. The EDS spectrum in Table 3 (FeOx29) shows abundances of Mg, Al, P, S, and Ni $\leq$ 1 at%.

We also studied Fe-O-Si smokes made by Nuth et al. (2000) shown in Fig. 9B. Here, amorphous and crystalline objects a few nm wide aggregated to produce smoke particles. The EDS overlay in the image shows that the Fe-O-Si elements are heterogeneously distributed, unlike in Andromeda oxides.

Kosmochloric Pyroxene

We observed a kosmochloric pyroxene (i.e., Na-Cr coupled substitution) in the FGM similar to those commonly found in other Wild 2 samples and in CP-IDPs (Joswiak et al. 2009). The elemental quantification is shown in Table 4 Px30. Small amounts of P and S in the spectrum may have been due to neighboring glassy material and neighboring sulfide. Its diffraction was consistent with diopside, as should be expected based on its composition. The Na content was 0.159 cations per 6 oxygens, which was well balanced by Ti^{4+}, Al^{3+} and Cr^{3+}: Al + Cr + 2Ti = 0.174 cations per 6 oxygens, suggesting (Ti, Al, Cr)-Na coupled substitution. A small sulfide-metal appendage was found on one side of the pyroxene (Table 1, Sulfide07). The Ni/Fe ratio was significantly larger than the primary sulfide impactor.

DISCUSSION

Wild 2 FGM Compared to IDPs

Hypervelocity capture of particles in aerogel can produce objects that are morphologically reminiscent of

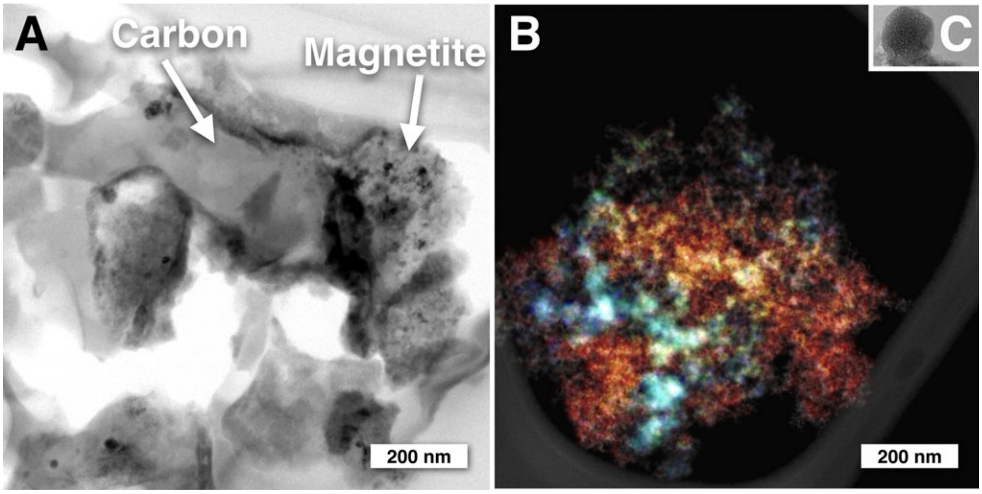

Fig. 9. A) BF image of magnetite from the IDP Lambda. B) LRGB image of Fe-smoke made by Nuth et al. (2000). Luminance channel is HAADF, Fe (red), O (green), Si (blue). C) An Fe oxide from FGM16 to scale for comparison. All scale bars are 200 nm.

GEMS (Hörz 2000; Okudaira et al. 2004; Burchell et al. 2006; Hörz et al. 2006; Noguchi et al. 2007; Ishii et al. 2008; Leroux et al. 2008a; Rietmeijer 2009b; Abreu et al. 2011; Leroux and Jacob 2013). Four common signatures distinguish these objects from GEMS. (1) Excess silica is usually present due to mixing with the aerogel. In some cases the original compositions are still preserved except for the excess SiO_2. (2) The rapid heating of sulfides reduces them to iron metal and subsequent rapid cooling recondenses the sulfur on the outside to form sulfide rims on the iron cores (Leroux et al. 2008b). (3) Vesicular structures from rapid volatilization are often observed. (4) Euhedral shapes on crystals, especially sulfides, are lost as they are liquified, volatilized, or ablated.

Keller and Messenger (2011) studied GEMS grains and noted that they had varying degrees of silicate polymerization. We examined the compositions of the GEMS-like and EA-like objects in a fashion modeled after Keller and Messenger (2011), see Fig. 7. Most of our objects show excess O, which is likely an artifact of the surrounding epoxy, so this analysis is not sensitive to the presence of OH. However, we find a very similar trend to that observed by Keller and Messenger (2011), namely these objects have a variable silicate polymerization between SiO_3 and SiO_4. Aerogel dilution would push the composition toward SiO_2, but the distribution of our objects does not favor compositions more silica-rich than SiO_3.

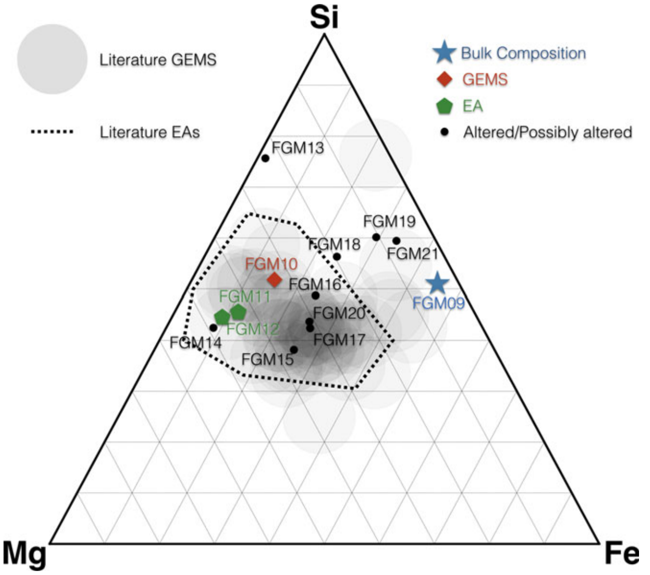

Fig. 10. Ternary plot showing the compositions of fine-grained materials in Andromeda compared to the GEMS field from Messenger et al. (2015), and EA field from Keller and Messenger (2009). SiO_2 enrichment from aerogel mixing would push all the points toward the Si corner. FGM09 is the bulk composition of the entire FGM region including many objects which are not GEMS or EAs.

In Fig. 10 we show the compositions of all the FGMs studied in Andromeda against literature values for GEMS compositions from Messenger et al. (2015) and EA compositions from Keller and Messenger (2009). The plot shows the importance of using both compositional data and petrographic data in order to classify the objects as GEMS or altered materials, since we have many objects which are compositionally consistent with GEMS in the ternary plot but are not likely to be pristine GEMS based on their morphology. With the exception of a few objects which we identified as likely altered, our data are not significantly shifted toward either the Si corner or the Fe corner which would be expected if the FGM objects we studied were mixed with aerogel or sulfide from the primary impactor grain. The bulk composition of the FGM is shifted toward the Si-Fe edge, which is consistent with some excess aerogel and/or sulfide in the FGM as a whole. In combination with other constraints on the contamination of the FGM (see supporting information), it is likely that not more than half of the material is aerogel + remelted sulfide from the leading edge of the impactor. This will be discussed in more detail below.

The compositions of GEMS measured by Keller and Messenger (2011) and Messenger et al. (2015) are shown in Fig. 11 as gray points. The Andromeda GEMS-like objects reported in this paper are also plotted in Fig. 11 and are consistent in elemental composition with GEMS. As expected, the bulk composition of the entire Andromeda FGM is not GEMS-like because it contains pyroxenes, sulfides, and other cometary objects as well as some potential excess SiO_2 and FeS from the capture process.

Aerogel Capture: Dynamics and Thermal Environment

Here, we characterize the stopping dynamics and thermal environment experienced by Andromeda during capture in aerogel. Following Dominguez (2009) and Trigo-Rodriguez et al. (2008), we assume a hydrodynamic model for hypervelocity aerogel capture—that is, the physics is identical to that of a projectile stopping in a gas (Fig. 12). This approach is justified because the hydrodynamic forces are much larger than the mechanical strength of the aerogel. In this regime, the range R of a spherical particle with radius r_g, density ρ, and initial speed v, stopping in aerogel with density ρ_a, is

$$R = \lambda r_g \ln \frac{v}{v_c} \tag{3}$$

where v_c is the speed at which the mechanical strength of the aerogel becomes important, which we take to be comparable to the sound speed in aerogel, ≈100 m s^{-1} (Dominguez 2009), and $\lambda = (4/3)(\rho/\rho_a)$.

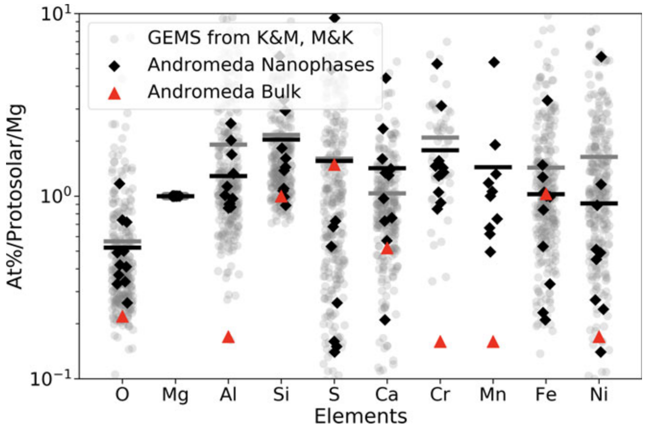

Fig. 11. Comparison of thermally modified and pristine GEMS-like and EA-like objects within Andromeda's fine grained material (FGM) to GEMS from literature. Black diamonds indicate Andromeda nanophase object compositions normalized to protosolar and Mg. Horizontal black bars are the mean composition. Gray circles indicate GEMS compositions from Keller and Messenger (2011) (K&M) and Messenger et al. (2015) (M&K). Horizontal gray bars are the GEMS mean composition. Red triangles show the bulk composition of the Andromeda FGM, which is distinctly not GEMS-like since it contains pyroxenes, sulfides, and other astromaterials.

This calculation underestimates the actual range, because it only calculates the distance from the aerogel surface to the transition away from hydrodynamic stopping. After this transition, stopping is dominated by the crushing strength of the aerogel. At 6 km s^{-1} capture speed, this residual range is short compared to the total range.

Because we have no information about the location of Andromeda within the original complex projectile—not to mention the difficulty of modeling the stopping of a complex, fragmenting particle in aerogel—we treat Andromeda as an isolated, robust, refractory object.

Andromeda was found at the end of the second longest of at least seven terminal subtracks identified in track 191 (Fig. 1), a large track near one edge of Stardust cometary tile C2086 ($\rho_a = 0.028$ g cm^{-3}). Since Andromeda is dominated by sulfide, we take $\rho = 4.6$ g cm^{-3}, so $\lambda \approx 220$. With $v_i = 6.1$ km s^{-1} and $r_g = 8\,\mu$m, the predicted range in this aerogel is 7.0 mm. The observed range was 8.8 mm, so the final ≈1.8 mm of the range was probably dominated by nonhydrodynamic stopping, but may have included a range increment if Andromeda was not located near the leading edge of the track 191 projectile, so that it was delayed in encountering the aerogel stopping medium.

We calculated that 70% of the speed and 90% of the kinetic energy were lost within the first 2 mm of penetration into the aerogel, within ≈0.6 µs after impact. This is the region in which most of the heating occurs. Because the projectile was hypersonic with Mach number ≫10, a strong shock just ahead of the leading edge of the projectile heated and vaporized the aerogel capture medium and the leading edge of the sulfide. In the case of a strong shock ($M \gg 1$), the postshock temperature and pressure are

$$T \sim \frac{2(\gamma-1)}{(\gamma+1)^2}\frac{m}{k}v^2 = \frac{5}{36}\frac{m}{k}v^2 \tag{4}$$

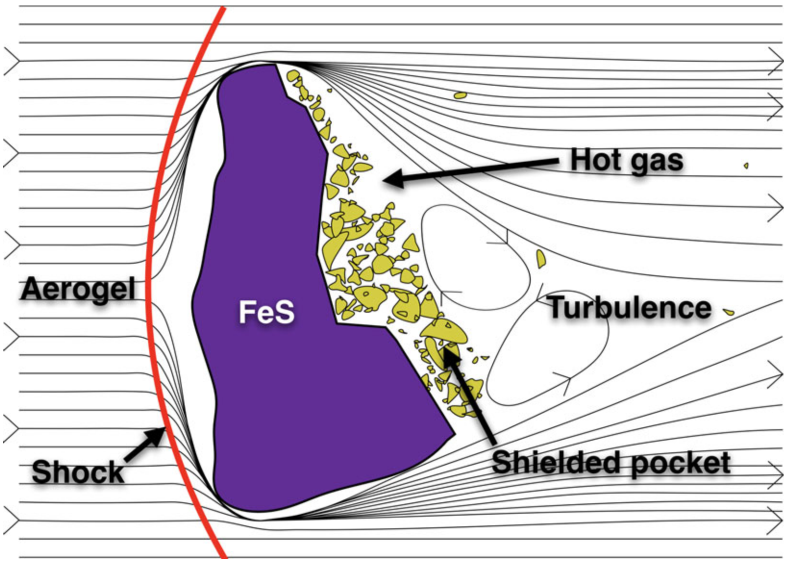

Fig. 12. Hypersonic flow during capture. Aerogel meets the face of Andromeda's sulfide producing a shock (red) that vaporizes aerogel and FeS. Hot SiO_2 and FeS gas flow around the particle. A turbulence region behind Andromeda causes some of the hot gas to enter the fine-grained material (FGM) and heat it. Some pockets of FGM are difficult to heat because they are shielded from the hot gas by other FGM. Primitive objects in these pockets can survive capture.

and

$$P \sim \frac{2}{\gamma+1}\rho_a v^2 = \frac{5}{6}\rho_a v^2 \qquad (5)$$

where m is the molecular mass, v is the velocity, ρ_a is the aerogel density, $\gamma = c_p/c_v$ is the adiabatic index, k is Boltzmann's constant, and $\sim$ indicates an order of magnitude relationship (Shu 1992). Here we assume an adiabatic index $\gamma = 1.4$. This postshock temperature corresponds to approximately 4 eV/molecule at maximum heating.

We assume a bulk aerogel temperature of ~ 200 K at the time of cometary dust capture. The impactor transfers energy that dissociates atoms and molecules from the aerogel and sulfide surface, and then heats the remaining solid and gas. We computed silicate and FeS dissociation energies using DFT and from thermodynamic parameterizations in the JANAF database and show the results in Table 5. If we further assume that the dissociation follows a Boltzmann distribution, i.e., $\exp^{-E_a/kT}$ where $kT = 4$ eV, and E_a is the dissociation energy computed by DFT, or derived from JANAF, then we expect one-quarter to one-third of the silica and FeS to dissociate into molecular SiO_2 and FeS. We also expect a few percent each of O_2, O, Si, Fe, and S. This will lead to very high oxygen and sulfur fugacities.

We computed the temperature of the hot gas at the shockwave. We started with the energy loss due to deceleration. We assumed that the energy is partitioned equally between FeS and aerogel, so ≈20% of the silica and ≈30% of the FeS are volatilized, in accordance with the dissociation fractions predicted from DFT. The remaining solids and gases are heated to higher temperature by the remaining available energy. The result is shown in Fig. 13. The initial gas temperature is about 14,000 K at the start of the impact but falls rapidly. The gas temperature falls to <1000 K by 2.5

Table 5. Dissociation energies and abundances from DFT and JANAF at 0 K.

Reaction	Energy (DFT, eV)	Dissociated % (DFT)	Energy (JANAF, eV)	Dissociated % (JANAF)
$SiO_2(s) \rightarrow SiO_2(g)$	6.5	20	6.2	21
$SiO_2(s) \rightarrow SiO(g) + O(g)$	12.1	5	10.9	7
$SiO_2(s) \rightarrow Si(g) + O_2(g)$	13.9	3	14.0	3
$SiO_2(s) \rightarrow Si(g) + 2O(g)$	22.5	0	19.1	1
$FeS(s) \rightarrow FeS(g)$	5.1	28	4.9	29
$FeS(s) \rightarrow Fe(g) + S(g)$	12.2	5	8.2	13

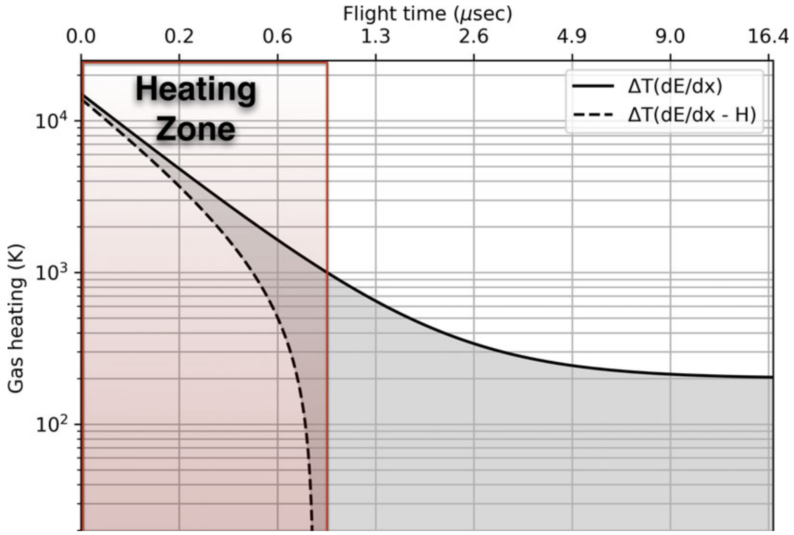

Fig. 13. Vaporized gas temperature as a function of time. The top solid line shows simple heating of gases and serves as an upper limit for the temperature. The bottom dashed curve heats the gases only after accounting for the heat used to volatilize aerogel and sulfide, as well as to dissociate $FeS(g) \rightarrow Fe(g) + S(g)$ and $SiO_2(g) \rightarrow SiO(g) + O(g)$ or $Si(g) + O_2(g)$. The bottom curve serves as a lower limit for the heating. The shaded region shows the range of possible temperatures as a function of depth per the model. The heating zone marks the region where gas temperatures exceed 1000 K and lasts for <1 μs and <3 mm into the track.

mm into the track after a time of <1 μs. We define this initial region as the heating region (see Fig. 13). Although this model makes a number of simplifying assumptions, the conclusion is clear: this particle was exposed to ≈ 10^4 K gas for <1 μs.

The inertia of the radially accelerated material and the pressure of the shocked gas were largely responsible for blowing the bulbous cavity in the aerogel (Fig. 1). The travel time from the surface of the aerogel to the end of the hydrodynamic regime was ≈17 μs (Fig. 13).

The heating of the sulfide and FGM in response to the < 1 μs thermal pulse depends on their respective thermal inertias. Given radius r, specific heat capacity c_p, density ρ, and thermal conductivity k, the thermal time constant τ is

$$\tau \sim \frac{\rho c_p}{k} r^2. \tag{6}$$

Using physical constants for sulfide from Tsatis and Theodossiou (1982), we find that the thermal time scale for Andromeda's sulfide was $\tau > 20$ μs. The thermal time constant τ of a particle describes the time required for it to heat up or cool down to $1/e$≈36% of the difference between its initial temperature and a new temperature. This was an order of magnitude longer than the duration of its exposure to 10^4 K gas and limits the internal heating it would have experienced. A 1-μs exposure to 10^4 K gas with a time constant of 20 μs leads to a maximum heating to ≈700 K, which assumes no heating losses from ablation. Within 1 μs after entering the aerogel, Andromeda was again in a cold environment, and frictional heating during stopping was negligible. There were undoubtedly ablative losses as the sulfide decelerated, and these would have removed heat from the sulfide, so the interior may have remained at a few hundred degrees for approximately its thermal time constant, ≈20 μs. This surficial heating is reminiscent of entry of large meteorites by the Earth's atmosphere.

The heating profile we calculate here is also consistent with literature pertaining to capture of larger grains. Noguchi et al. (2007) found that heating duration was between 0.1 and 1.8 μs based on thermal profiles of phyllosilicates shot into aerogels with light gas guns.

High-Ni Bands in Sulfide: Indicator of Preaccretional Heating?

The primary impactor was troilite with narrow Ni-rich bands of pyrrhotite 4C. In the case of the three bands averaged in Fig. 4, we computed the width by assuming stoichiometry. First we assumed (Fe+Ni)/S = 1 outside the Ni-rich bands, and then calculated (Fe+Ni)/S = 0.994 at the center of the bands. Pyrrhotite 4C has (Fe+Ni)/S = 0.875. Since the resolution of the EDS map was 30 nm, the pyrrhotite bands should have been ≤ 2 nm or one to two unit cells thick (in the c* direction) and would have had a composition of Fe_6NiS_8 (Table 1, Sulfide06) to yield the observed composition. Such a thin band would have produced a broadening of the diffraction reflections of $\approx 1\ \mathrm{nm}^{-1}$. Based on SAED we found the peak broadening of the 4C superlattice reflections to be only $0.28\ \mathrm{nm}^{-1}$, which could be produced by bands on the order of 6–7 nm thick. Some regions of the sulfide had Ni content as high as 1 at% (i.e., double the Ni content in Fig. 4) and the HRTEM image shown in Fig. 3 shows a Ni band more than 20 nm thick. The likely explanation is that the sulfide contained Ni-rich pyrrhotite bands of varying thickness averaging around 7 nm.

Gainsforth et al. (2017b) related the broadening of pyrrhotite 4C superlattice reflections with varying degrees of disequilibrium. If the sulfide is a nebular condensate (e.g., formed at 773 K), then the disorder would record the initial formation conditions. We follow the discussion of Gainsforth et al. (2017b), based on the experimental sulfidation of metal foils using H_2S by Lauretta (2005). Andromeda's $[\mathrm{Ni/Fe}]_{\odot} = -1.3$ implies a large depletion of Ni in the source material or a very low partition of Ni into the sulfide phase. During sulfidation of Fe-metal by H_2S at 773 K, Ni partitions primarily into the metal phase and forms taenite or can be pulled into schreibersite if P is present. Lower formation temperatures lower the partitioning of Ni into the sulfide but formation out of equilibrium favors placing more Ni into the sulfide. At 773 K, for pyrrhotites showing a similar level of disorder, and for "nebular metal" with a few at % Ni, Cr, P, and C, we expect a partition between metal and sulfide $D^{\mathrm{Ni/Fe}}_{\mathrm{metal/FeS}} = 1\text{–}2$. Therefore, this sulfide did not form under these conditions because its Ni content is one order of magnitude too low. It could have formed under cooler temperatures but for a longer time so as to achieve a similar proximity to equilibrium. At 673 K, $D^{\mathrm{Ni/Fe}}_{\mathrm{metal/FeS}} = 5$. This would still put two to three times too much Ni into the sulfide. Alternately, it could have formed from a Ni-poor metal having only 0.1–0.5% Ni originally.

Another possibility is that Andromeda's sulfide is not a primary nebular condensate but rather formed in an igneous environment or experienced a metamorphic event. The fact that the Ni has partitioned into well-defined Ni-rich bands suggests that it was homogeneously dissolved throughout the sulfide at an earlier time, but later conditions pushed it out of equilibrium. Such a condition could be obtained from a metamorphic event.

To understand the thermal history, we need to know what thermal profile could have exsolved the pyrrhotite. To our knowledge, the diffusion rate of Ni as a function of temperature in troilite has not been measured. Condit et al. (1974) measured the diffusion rates of Fe in troilite and pyrrhotite over the temperature range of 500–1000 K. We computed the time scales for diffusion of Ni by assuming it to have the same diffusivity as Fe. At 500 K, the segregation might occur on the time scale of hours and at 1000 K it could occur on the time scale of 1 s. We did not extrapolate to temperatures below 413 K because of a phase transition at that temperature.

We previously calculated that the sulfide was heated to no more than several hundred degrees for a few µs during aerogel capture, so diffusion is far too slow to have allowed the Ni-rich bands to form as a result of capture in aerogel. We conclude that the bands are an original feature, either dating from initial formation or are due to low-temperature metamorphism.

High-Ni lamellae from meteoritic sulfides with these characteristics have not been reported previously. In previous analyses with similar sensitivity of four large Wild 2 sulfides, no such lamellae were observed. This provides further evidence against an aerogel capture origin, and also points to a diversity in formation/alteration history of sulfides within Wild 2. It is worth noting that the small variation in Ni content is very difficult to see instrumentally. The lack of reports in the literature may be due to the fact that TEM instruments capable of seeing this phenomenon easily have only recently become available. Our initial map of Andromeda missed the Ni-banding—it was only after we acquired a high count map with $>10^8$ counts, for Se quantification, that the bands became obvious. As high-count EDS systems become more abundant in the community, more such banded sulfides may be found.

FGM Porosity, Density, Modal Abundance

Here we compare the physical characteristics of the FGM to FGM in CP-IDPs and to in situ cometary observations.

We estimated the porosity (ϕ = fraction of filled space) of the FGM from Si and S EDS maps. We could not determine the modal abundance of carbonaceous material because of the ubiquitous epoxy. We found $\phi = 0.57$ for the FGM. Eighty-eight percent of the material in the FGM was silicate and 12% of the material was sulfide, so we estimated the bulk density of the FGM to be $\approx 1.4\ \mathrm{g\ cm}^{-3}$.

Gainsforth et al. (2017a) found porosities and densities for several IDPs and found values in approximate agreement with Andromeda. Specifically, the porosity, density, and silicate/sulfide abundance of the FGM is comparable to the silicate/sulfide abundance in the "Nessie" IDP (L2071 Cluster 17). Joswiak et al. (2005) also reported densities of $0.7\text{–}1.7\ \mathrm{g\ cm}^{-3}$ for several TEM sections of IDPs, and Fraundorf et al. (1982) reported densities of $0.7\text{–}2.2\ \mathrm{g\ cm}^{-3}$ for IDPs measured on a quartz fiber balance. As noted in Gainsforth et al. (2017a), measurements from the

Rosetta mission using the GIADA instrument found that dust grains ejected from Comet 67P/Churyumov-Gerasimenko (C-G) had densities between 1 and 3 g cm^3 (Rotundi et al. 2015).

Using high-precision Doppler measurements, the Rosetta mission was able to measure the mass of 67P/Churyumov-Gerasimenko nucleus (Sierks et al. 2015). This yields a density of 0.5 g cm^{-3}. The discrepancy between this bulk measurement of the comet nucleus and the higher densities seen in CP-IDPs and C-G particles implies the existence of void spaces on a larger length scale than the size of CP-IDPs or cometary particles collected by Stardust.

FGM Heating

As discussed earlier, vaporized aerogel and sulfide gas would have been in thermal contact with the leading edge of the particle. Unless the particle was rotating very rapidly ($\approx 10^6$ rotations s^{-1}), Andromeda did not rotate significantly during the 1 μs hot thermal pulse, so one side was a leading edge and the opposite side a trailing edge. The FGM in the sulfide embayment was likely on the trailing edge of the sulfide during capture in aerogel. The hydrodynamic pressure (>1 GPa on the leading edge) was probably much larger than the binding strength between the FGM particles, so it is unlikely that this loosely bound material would have survived intact if it had been exposed directly to the flow of hot, vaporized gas.

In the Results section, we reported evidence of variable heating of individual silicate particles in the FGM. Here we explore three possible heating mechanisms, related to aerogel capture.

The most likely mechanism was direct thermal contact with gas from the shocked, vaporized mixture of aerogel and ablated upstream cometary materials. Cooler gas in the cavitation region of the supersonic flow could have penetrated the porous FGM and been in thermal contact with it for the duration of the <1 μs hot pulse (Fig. 12). Near the top of the track, the SiO_2 gas would have been partially dissociated into SiO and O, and the FeS gas would have been partially dissociated into Fe and S, so it would have been oxidizing and sulfidizing. The thermal time constant of $\approx$300 nm silicates is small, $\ll$0.1 μs, so any particles exposed to the gas would have rapidly equilibrated with it, but variations in permeability of the porous FGM could be expected to lead to variable exposures to the hot gas. We would expect some regions of the FGM to be inaccessible to the gas and any GEMS, EAs, or other primary objects in these "shielded pockets" would be unheated or minimally heated, and remain unoxidized and unsulfidized. Without more information about the permeability and porosity of the FGM, it is probably not possible to model this process with sufficient fidelity to compare with detailed observations.

We also considered radiative heat transfer from a hot, ionized gas, conservatively assuming that the radiating gas was an optically thick blackbody, and the FGM was also a blackbody with 100% absorptivity. We calculated that the heating of FGM was less than 1 K and rule it out as a significant heating mechanism.

Finally, we consider heating due to contact with liquid phase SiO_2 or FeS entrained in the gas flow and entering the FGM. Excess silica is a common indicator of aerogel mixing in the bulb region of Stardust tracks (Leroux et al. 2008a; Stodolna et al. 2012a). Whether molten material could damage neighboring FGM depends on the presence of direct contact with the FGM. As shown above, blackbody radiative transfer is ineffective at transferring heat under the conditions of capture, so if significant heat transfer does occur it should be via direct contact—i.e., phonon transmission. Since the FGM is highly porous, the heat is likely to dissipate through a complex network of "heat pipes" formed by connected molten material. See Bouquerel et al. (2012) for a discussion of how phonon transmission affects thermal conductivity in aerogel. Random positioning of nanophases within voids of this network would determine the degree of heating and alteration they could experience. Future work may improve our understanding of contact heat transfer in Stardust FGM, but for the time being it is clear that such heat transfer did not destroy all the FGM because objects exist which have the petrographic and chemical signatures of survival. For material in these pockets, contact with hot gas is likely the dominant mechanism for heating.

To address heating due to contact with hot gas, we computed the heating that would be experienced by 200 K quartz (as a proxy for FGM) from thermal equilibration with an SiO_2 gas at 10^4 K. Assuming the gas/solid ratio is 1%, we found that the FGM should heat to $\approx$300 K. If the abundance of gas was an order of magnitude greater, then the FGM could have heated to about 1100 K, which is high enough to begin to see alteration—though only the smallest objects (e.g., GEMS) would alter on the time scale of 1 μs. It is also possible that the hot gas heated a smaller fraction of the material because it was only in contact with material accessible through large pores. Indeed, if we assume that the gas was only in contact with about 10% of the FGM, then it should have heated about 10% of the FGM to destructive levels.

These findings are in agreement with earlier experimental studies. Noguchi et al. (2007) found that aerogel capture of particles creates a high temperature gradient at the heating interface in the range of 10^3 K/μm and found that this implied cooling times <2 μs, which is consistent with our estimates from gas heating.

Objects located in the bulbs or tracks away from the terminal region may not be so lucky because the cometary mass can be outweighed by the mass of molten aerogel. Roskosz et al. (2008) found that large micron sized grains could be amorphized. Diffusion profiles indicated that some of these grains experienced heating up to 2100 K for 100 μs. However, rapid heating and cooling does not produce crystalline phases, with the exception of the Fe and FeS nanobeads seen in GEMS-like particles which are only a few nm across (Noguchi et al. 2007; Ishii et al. 2008; Stodolna et al. 2012b).

Brownlee et al. (2005) found that heating GEMS to temperatures $\geq$1000 K for several hours results in subsolidus crystallization of the silicate and they postulated that equilibrated aggregates could have formed by heating in the nebular environment. If this picture is correct, then equilibrated aggregates should be more robust to transient heating events than GEMS—i.e., GEMS should be more susceptible to destruction during aerogel capture than equilibrated aggregates. With this in mind, the survival of a GEMS would provide the strongest constraint on the temperatures during heating.

Primitive FGM

FGM10 is the best candidate for a GEMS in Andromeda (Fig. 5). It contains euhedral sulfides, does not contain excess silica, and retains the expected chemical composition of a GEMS. While there is likely some heating on one side of FGM10 where there is one subhedral external sulfide, and sulfur has bled into the silicate matrix, the appearance of FGM10 is similar to GEMS seen in IDPs, many of which also show evidence of heating from atmospheric entry or nebular events (Brownlee et al. 1993; Dai and Bradley 2005). FGM10 is indistinguishable in its characteristics with GEMS in CP-IDPs. For example, see fig. 5 in Keller and Messenger (2005) or fig. 1 in Keller and Messenger (2011).

FGM11 and FGM12 appear to be indistinguishable from equilibrated aggregates in CP-IDPs, with no indicators of shock heating from the aerogel capture. Equilibrated aggregates are probably more robust to heating than GEMS and so it is possible that they were heated but not modified by the process. For comparison to EAs in IDPs, see fig. 2 in Rietmeijer (2009a), fig. 2 in Keller and Messenger (2005), or fig. 1 in Keller and Messenger (2009).

Altered FGM

We argue that the remaining nanophases studied in Andromeda's FGM were thermally altered to a greater or lesser degree on account of the presence of one or more of the heating indicators we described in the previous sections.

FGM20 was especially noteworthy because EDS imaging could clearly distinguish euhedral grains of distinct compositions but bright field imaging and diffraction indicated the grains were amorphous. We interpret this as similar to "shadow grains" described previously by Stodolna et al. (2012a) and Leroux et al. (2008a) when a crystalline phase is amorphized by rapid heating and cooling but not sufficiently heated for the atoms to diffuse away. The atoms then settle into metastable amorphous phases with shapes and compositions very close to their original crystalline counterparts.

FGM20 was in contact with the primary impactor sulfide in a region containing many Fe oxides, and did not show excess silica. Because it was found in a central part of the FGM, it would have been unlikely that it came into contact with hot, molten aerogel. Instead, its morphology was consistent with the hot gas model we propose. If hot gas permeated the FGM, then it could have penetrated all open pores and come in contact with the sulfide where it would have rapidly cooled.

Amorphous FeO_x

The amorphous Fe oxides found near FGM16 (Fig. 7), FGM17, and FGM20 may be important to understanding the origin of the FGM. The oxide is embedded in epoxy, so it is not possible to determine the exact oxygen abundance even after subtracting off a background epoxy spectrum. However, based on rough stoichiometry, we expect a minimum oxidation of Fe^{2+}, and in some cases more oxygen is present than would be expected for Fe^{3+} so even oxy-hydroxide is consistent with our error margin. Other rock-forming elements are present in lower abundance.

The Fe oxide is closest in composition to magnetite rims in some mildly heated IDPs. In such IDPs it is possible to find magnetite rims on the order of 100 nm, which contain nanocrystalline and amorphous oxidized Fe. These often contain small abundances of other elements deriving primarily from the neighboring sulfides and silicates from which they formed. The oxides in Andromeda all contain significant abundances of other elements, but Si and S are present in every spectrum and furthermore are present in roughly equal amounts of a few At%.

Bridges et al. (2010) found amorphous FeO_x within track bulbs. TEM analysis of one oxide from C2005,2,121,1,0 showed that it was amorphous and approximately 0.5 μm across—comparable to the oxides we see. XANES of other oxides showed that much of the Fe was oxidized and Raman was suggestive of magnetite/hematite. Some of these oxides could have a similar origin to the oxides we see in Andromeda's FGM if they were formed by gas-phase condensation.

Experiments by Nuth et al. (2000), Rietmeijer and Nuth (2000), and Abreu et al. (2011) have shown that it is possible to synthesize Fe oxide amorphous nanoparticles directly from the vapor phase in an ≈ 90 Torr H_2-rich gas (0.12 bar). They were formed at 500–1500 K and on time scales "much less than a second." With the exception of the H_2 atmosphere and the low pressures, these conditions are consistent with what we should expect from shock heating during aerogel capture.

Figure 9 shows nanocrystalline magnetite in an IDP alongside artificial smokes produced by Nuth et al. (2000). The inset shows an Fe oxide from Andromeda for comparison (also cf. Fig. 7).

Barth et al. (2017) show that at lower temperatures, e.g., 450°C, Fe oxides can form from a high f_{O_2} and high f_{S_2} gas. Specifically under high fugacity, low temperature conditions, oxides are stable unless $\log(f_{O_2}) < \log(f_{S_2})$ by about 20 log units. Our calculations above show that log $(f_{O_2}) \approx \log(f_{S_2})$, which means that hematite would have been the stable phase if aerogel + sulfide gas were condensing. Because the process would have been so rapid, the Fe oxide would not have crystallized but instead solidified as an amorphous solid.

The prevalence of Fe oxide at the interface between the large sulfide impactor and the FGM would have been expected. Because the sulfide did not have time to heat up more than a few hundred degrees during the capture process, it should have acted as a heat sink for nearby material. As hot gas permeated through the FGM and came into contact with the sulfide, it would have cooled to a few hundred degrees, which would have driven rapid condensation. Hot gas further out in the FGM would have diffused out of the FGM at a later point and would likely leave less residue.

Wild 2 as an Aggregate Rock

Immediately after the Stardust return, Brownlee et al. (2006) proposed that comet Wild 2 is, effectively, an aggregate of inner and outer solar system materials which indicated substantial mixing throughout the solar nebula. The amount of presolar material present in Wild 2 is consistent with CP-IDPs, and other primitive bodies (Floss et al. 2013), so Wild 2 is certainly sampling some unaltered solar nebula material. Work on large rocky objects (terminal particles) in Wild 2 has frequently identified chondrules, and refractory rocks indicating that inner solar system materials composed a significant fraction of the captured mass of Wild 2 (Nakamura et al. 2008; Joswiak et al. 2012; Brownlee 2014; Gainsforth et al. 2015a). Recently, Joswiak et al. (2017) found that calcium-aluminum-rich inclusion (CAI)-like fragments account for ≈1 vol% in cometary samples including Wild 2 and a giant cluster IDP named U2-20GCP. Joswiak et al. (2017) make a strong case that U2-20 has a cometary origin, and have noted (personal communication) that it has coarse-grained rocks (CAI-like) in direct contact with FGM including GEMS and EAs. Wooden et al. (2017) recently tied together several lines of evidence pointing to late formation of Wild 2 materials, several Mya the onset of CAI formation. These include an abundance of objects with O isotopic signatures close to the terrestrial value, and an overabundance of late stage objects including Fe-rich type II chondrules, and late ^{26}Al dates (Ogliore et al. 2012, 2015). Wild 2 olivines also show some evidence of having been metamorphosed (Frank et al. 2014).

Nevertheless, while Wild 2 FGM has occasionally been found near large terminal particles, the FGM has usually been heavily altered and as a consequence, comparison with FGM in CP-IDPs has been difficult. For example, the only enstatite whisker found to date in Wild 2 is encased in glass—a phenomenon never reported previously (Stodolna et al. 2014). Febo (C2009,2,57) has had to date the most promising FGM, but significant unresolved questions about the alteration of the FGM remain (Joswiak et al. 2012). A long-standing open question has therefore been whether Wild 2 has any "CP-IDP" FGM at all. The fortuitous survival of particles in the Andromeda FGM indicates that the answer is "yes."

The presence of sulfides in the FGM with a significantly different composition than the impactor indicates that they are not simply ablation products from the impactor during capture. This means that the FGM does not share the same formation/alteration history that Andromeda's large sulfide experienced. If the sulfide had been metamorphosed while aggregated to the FGM, the FGM would not have survived, so either the sulfide formed originally with Ni-rich bands, or aggregated with the FGM after metamorphosis/nebular heating. This observation supports the conclusion that Wild 2 is an aggregate rock with GEMS and equilibrated aggregates alongside larger rocks/minerals.

K and P are volatile elements and are present in nearly all the objects within the FGM material that we studied, and may provide another window into the relationship between the FGM and the coarse material. Because of their volatility, the gas heating model would predict that K and P would disperse throughout the FGM with the gas and then recondense as the gas cooled. However, K is significantly enriched in the bulk composition with $[K/Si]_{\odot} = 0.32$. Simple redistribution of K would predict that the bulk would remain unchanged or even depleted as K escaped into the nearby aerogel. High K has been noted previously within Stardust samples (Flynn et al. 2006), though there is some evidence for K as an occasional contaminant in aerogel alongside Cl and Ca (Rietmeijer 2015). K is especially intriguing as it is commonly enriched in more evolved materials. The carrier phase for the K in Andromeda has not been identified and may have been destroyed during capture. This suggests that an investigation of the abundance and carrier of K in CP-IDPs may yield interesting results.

P, on the other hand, is not particularly enriched in the bulk FGM ($[P/Si]_{\odot} = 0.049 \approx 0$), but is significantly overabundant around the nanophases we investigated (typical $[P/Si]_{\odot} = 0.15$ with the highest value at FGM21 with $[P/Si]_{\odot}) = 0.55$). The nanophases we investigated were preferentially those which looked like GEMS or EAs or other primitive material (i.e., not large crystals, sulfides, etc.). Therefore, while FGM21 shows that P was likely redistributed to some degree during capture, it must also be more concentrated within the GEMS/ EA-type objects or else it would have also been more concentrated in the bulk. The reason for this is not clear but warrants investigation in the future.

CONCLUSIONS

We summarize key conclusions.

1. Wild 2 contains objects that are indistinguishable from GEMS and equilibrated aggregates found in CP-IDPs.
2. Wild 2 is an aggregate containing both large crystals and FGM.
3. Ni banding in the sulfide impactor may show evidence for heating between formation and incorporation into comet Wild 2.
4. The distribution of K and P leads us to suggest that future research would benefit by identifying the origin and chemistry of K- and P-bearing phases in IDPs.

We have also constrained the processes active during Andromeda's capture, which allows us to better resolve which processes can be attributed to cometary/solar system processes and which are artifacts of capture. We demonstrate that objects within the FGM behind the sulfide impactor were heated by a transient hot gas on the order of $\approx 10^4$ K but for 1 μs at most. This is sufficient to melt individual silicates but some objects appear to have survived in a relatively pristine condition. This is likely due to variations in the porosity and the thermal inertia of nearby objects (e.g., the impactor and large crystalline grains), which shielded some FGM from exposure to the hot gas. The FGM only has excess aerogel in select regions. We have identified the gas-phase condensation of Fe oxide from volatilized Fe and O produced during aerogel capture.

Acknowledgments—Work at the Molecular Foundry and Advanced Light Source was supported by the Office of Science, Office of Basic Energy Sciences, of the U.S. Department of Energy under Contract No. DE-AC02-05CH11231. This work was supported under the LARS program by NASA grant NNX16AK14G. M. Z. was supported by NASA's Emerging Worlds Program.

We thank the staff at Johnson Space Center for making IDPs and Stardust samples available to the community. We also thank Karen Bustillo and the rest of the staff at the National Center for Electron Microscopy for providing spectacular instrumentation without which this paper would not exist. Finally, we thank Yufeng Liang and David Prendergast at the Molecular Foundry for tutelage with DFT and access to computing resources, Natasha Johnson and Joseph A. Nuth III for supplying the Fe smokes used for comparison with Fe oxides, and Lindsay Keller and an anonymous reviewer for excellent reviews that greatly improved the paper.

Editorial Handling—Dr. Edward Cloutis

REFERENCES

Abreu N. M., Rietmeijer F. J. M., and Nuth J. A. 2011. Understanding the mechanisms of formation of nanophase compounds from Stardust: Combined experimental and observational approach. *Meteoritics & Planetary Science* 46:1082–1096.

Arthur D. and Vassilvitskii S. 2007. k-means++: The advantages of careful seeding. Proceedings of the eighteenth annual ACM-SIAM symposium on discrete algorithms. pp. 1027–1035.

Barth M. I. F., Harries D., Langenhorst F., and Hoppe P. 2017. Sulfide-oxide assemblages in Acfer 094-Clues to nebular metal-gas interactions. *Meteoritics & Planetary Science* 53:187–203.

Black D. and Long G. 2004. *X-ray topography, SP 960-10*. Washington, D.C.: US Government Printing Office.

Bouquerel M., Duforestel T., Baillis D., and Rusaouen G. 2012. Heat transfer modeling in vacuum insulation panels containing nanoporous silicas—A review. *Energy & Buildings* 54:320–336.

Bridges J. C., Burchell M. J., Changela H. C., Foster N. J., Creighton J. A., Carpenter J. D., Gurman S. J., Franchi I. A., and Busemann H. 2010. Iron oxides in comet 81P/ Wild 2. *Meteoritics & Planetary Science* 45:55–72.

Brownlee D. 2014. The Stardust Mission: Analyzing samples from the edge of the solar system. *Annual Review of Earth and Planetary Sciences* 42:179–205.

Brownlee D. E., Joswiak D. J., Love S. G., Nier A. O., Schlutter D. J., and Bradley J. P. 1993. Identification of cometary and asteroidal particles in stratospheric IDP collections. Proceedings, 24th Lunar and Planetary Science Conference. pp. 205–206.

Brownlee D. E., Joswiak D. J., Bradley J. P., Matrajt G., and Wooden D. H. 2005. Cooked GEMS—Insights into the hot origins of crystalline silicates in circumstellar disks and the cold origins of GEMS. 36th Lunar and Planetary Science Conference. p. 2391.

Brownlee D., Tsou P., Aléon J., Alexander C. M. O., Araki T., Bajt S., Baratta G. A., Bastien R. K., Bland P., Bleuet P., Borg J., Bradley J. P., Brearley A., Brenker F., Brennan S., Bridges J. C., Browning N. D., Brucato J. R., Bullock E., Burchell M. J., Busemann H., Butterworth A. L., Chaussidon M., Cheuvront A., Chi M., Cintala M. J., Clark B. C., Clemett S. J., Cody G., Colangeli L., Cooper G., Cordier P., Daghlian C., Dai Z. R., D'Hendecourt L., Djouadi Z., Dominguez G., Duxbury T., Dworkin J. P., Ebel D. S., Economou T. E., Fakra S., Fairey S. A. J., Fallon S., Ferrini G., Ferroir T., Fleckenstein H., Floss C., Flynn G. J., Franchi I. A., Fries M., Gainsforth Z., Gallien J.-P., Genge M., Gilles M. K., Gillet P., Gilmour J., Glavin D. P., Gounelle M., Grady M. M., Graham G. A., Grant P. G., Green S. F., Grossemy F., Grossman L., Grossman J. N., Guan Y., Hagiya K., Harvey R., Heck P., Herzog G. F., Hoppe P., Hoerz F., Huth J., Hutcheon I. D., Ignatyev K., Ishii H., Ito M., Jacob D., Jacobsen C., Jacobsen S., Jones S., Joswiak D., Jurewicz A., Kearsley A. T., Keller L. P., Khodja H., Kilcoyne A. L. D., Kissel J., Krot A., Langenhorst F., Lanzirotti A., Le L., Leshin L. A., Leitner J., Lemelle L., Leroux H., Liu M.-C., Luening K., Lyon I., MacPherson G., Marcus M. A., Marhas K., Marty B., Matrajt G., McKeegan K., Meibom A., Mennella V., Messenger K., Messenger S., Mikouchi T., Mostefaoui S., Nakamura T., Nakano T., Newville M., Nittler L. R., Ohnishi I., Ohsumi K., Okudaira K., Papanastassiou D. A., Palma R., Palumbo M. E., Pepin R. O., Perkins D., Perronnet M., Pianetta P., Rao W., Rietmeijer F. J. M., Robert F., Rost D., Rotundi A., Ryan R., Sandford S. A., Schwandt C. S., See T. H., Schlutter D., Sheffield-Parker J., Simionovici A. S., Simon S., Sitnitsky I., Snead C. J., Spencer M. K., Stadermann F. J., Steele A., Stephan T., Stroud R., Susini J., Sutton S. R., Suzuki Y., Taheri M., Taylor S., Teslich N., Tomeoka K., Tomioka N., Toppani A., Trigo-Rodríguez J. M., Troadec D., Tsuchiyama A., Tuzzolino A. J., Tyliszczak T., Uesugi K., Velbel M., Vellenga J., Vicenzi E., Vincze L., Warren J., Weber I., Weisberg M., Westphal A. J., Wirick S., Wooden D., Wopenka B., Wozniakiewicz P., Wright I., Yabuta H., Yano H., Young E. D., Zare R. N., Zega T., Ziegler K., Zimmerman L., Zinner E., and Zolensky M. E. 2006. Comet 81P/Wild 2 under a microscope. *Science* 314:1711–1716.

Burchell M., Fairey S., Wozniakiewicz P., Brownlee D. E., Hoerz F., Kearsley A. T., See T. H., Tsou P., Westphal A. J., Green S., Trigo-Rodriguez J. M., and Dominguez G. 2008. Characteristics of cometary dust tracks in Stardust aerogel and laboratory calibrations. *Meteoritics & Planetary Science* 43:23–40.

Burchell M. J., Graham G., and Kearsley A. 2006. Cosmic dust collection in aerogel. *Annual Review of Earth and Planetary Sciences* 34:385–418.

Chase M. W. J. 1998. NIST-JANAF Thermochemical Tables Fourth Edition. *Journal of Physical and Chemical Reference Data*. Monograph 9:1–61.

Cliff G. and Lorimer G. W. 1975. The quantitative analysis of thin specimens. *Journal of Microscopy* 103: 203–207.

Condit R. H., Hobbins R. R., and Birchenall C. E. 1974. Self-diffusion of iron and sulfur in ferrous sulfide. *Oxidation of Metals* 8:409–455.

Corso A. D. 2014. Pseudopotentials periodic table: From H to Pu. *Computational Materials Science* 95:337–350.

Dai Z. R. and Bradley J. P. 2005. Origin and properties of GEMS (glass with embedded metal and sulfides). *Chondrites and the Protoplanetary Disk* 341:668–674.

Dominguez G. 2009. Time evolution and temperatures of hypervelocity impact-generated tracks in aerogel. *Meteoritics & Planetary Science* 44:1431–1443.

Floss C., Stadermann F. J., Kearsley A. T., Burchell M. J., and Ong W. J. 2013. The abundance of presolar grains in Comet 81P/Wild 2. *The Astrophysical Journal* 763:140–11.

Flynn G. J., Bleuet P., Borg J., Bradley J. P., Brenker F. E., Brennan S., Bridges J., Brownlee D. E., Bullock E. S., Burghammer M., Clark B. C., Dai Z. R., Daghlian C. P., Djouadi Z., Fakra S., Ferroir T., Floss C., Franchi I. A., Gainsforth Z., Gallien J.-P., Gillet P., Grant P. G., Graham G. A., Green S. F., Grossemy F., Heck P. R., Herzog G. F., Hoppe P., Hoerz F., Huth J., Ignatyev K., Ishii H. A., Janssens K., Joswiak D., Kearsley A. T., Khodja H., Lanzirotti A., Leitner J., Lemelle L., Leroux H., Luening K., MacPherson G. J., Marhas K. K., Marcus M. A., Matrajt G., Nakamura T., Nakamura-Messenger K., Nakano T., Newville M., Papanastassiou D. A., Pianetta P., Rao W., Riekel C., Rietmeijer F. J. M., Rost D., Schwandt C. S., See T. H., Sheffield-Parker J., Simionovici A. S., Sitnitsky I., Snead C. J., Stadermann F. J., Stephan T., Stroud R. M., Susini J., Suzuki Y., Sutton S. R., Taylor S., Teslich N., Troadec D., Tsou P., Tsuchiyama A., Uesugi K., Vekemans B., Vicenzi E. P., Vincze L., Westphal A. J., Wozniakiewicz P., Zinner E., and Zolensky M. E. 2006. Elemental compositions of Comet 81P/Wild 2 samples collected by Stardust. *Science* 314:1731–1735.

Frank D. R., Zolensky M. E., and Le L. 2014. Olivine in terminal particles of Stardust aerogel tracks and analogous grains in chondrite matrix. *Geochimica et Cosmochimica Acta* 142:240–259.

Fraundorf P., Hintz C., Lowry O., Mckeegan K. D., and Sandford S. A. 1982. Determination of the mass, surface density, and volume density of individual interplanetary dust particles (abstract). 8th Lunar Science Conference. p. 225.

Gainsforth Z. 2016. Stoichiometry fitter, a GUI for fitting solid solutions and analyzing mineral phases. *Microscopy and Microanalysis* 22:1808–1809.

Gainsforth Z., Brenker F. E., Simionovici A. S., Schmitz S., Burghammer M., Butterworth A. L., Cloetens P., Lemelle L., Tresserras J.-A. S., Schoonjans T., Silversmit G., Solé V. A., Vekemans B., Vincze L., Westphal A. J., Allen C., Anderson D., Ansari A., Bajt S., Bastien R. K., Bassim N., Bechtel H. A., Borg J., Bridges J., Brownlee D. E., Burchell M., Changela H., Davis A. M., Doll R., Floss C., Flynn G., Fougeray P., Frank D. R., Grün E., Heck P. R., Hillier J. K., Hoppe P., Hudson B., Huth J., Hvide B., Kearsley A., King A. J., Lai B., Leitner J., Leroux H., Leonard A., Lettieri R., Marchant W., Nittler L. R., Ogliore R., Ong W. J., Postberg F., Price M. C., Sandford S. A., Srama R., Stephan T., Sterken V. J., Stodolna J., Stroud R. M., Sutton S., Trieloff M., Tsou P., Tsuchiyama A., Tyliszczak T., Von Korff J., Zevin D., Zolensky M. E., and >30,000 Stardust@home dusters.

2013a. Stardust Interstellar Preliminary Examination VIII: Identification of crystalline material in two interstellar candidates. *Meteoritics & Planetary Science* 49:1645–1665.

Gainsforth Z., McLeod A. S., Butterworth A. L., Dominguez G., Basov D., Keilmann F., Thiemens M., Tyliszczak T., and Westphal A. J. 2013b. Caligula, a Stardust sulfide-silicate assemblage viewed through SEM, nanoFTIR, and STXM (abstract #2332). 44th Lunar and Planetary Science Conference. CD-ROM.

Gainsforth Z., Bustillo K., Butterworth A. L., Ogliore R. C., and Westphal A. J. 2014a. Trace element analysis in geochemical systems by STEM/EDS. *Microscopy and Microanalysis* 20-S3:1682–1683.

Gainsforth Z., Ogliore R. C., Bustillo K., Westphal A. J., and Butterworth A. L. 2014b. Ni zoned nano-pyrrhotite from Stardust Track C2062,2,152 (Cecil) (abstract #2637). 45th Lunar and Planetary Science Conference. CD-ROM.

Gainsforth Z., Butterworth A. L., Stodolna J., Westphal A. J., Huss G. R., Nagashima K., Ogliore R., Brownlee D. E., Joswiak D., Tyliszczak T., and Simionovici A. S. 2015a. Constraints on the formation environment of two chondrule-like igneous particles from comet 81P/Wild 2. *Meteoritics & Planetary Science* 50:976–1004.

Gainsforth Z., Butterworth A. L., and Westphal A. J. 2015b. Unequilibrated spinels in Stardust Track C2062,2,162 (Cecil). *Meteoritics & Planetary Science* 46:2974.

Gainsforth Z., Jilly-Rehak C. E., Butterworth A. L., and Westphal A. J. 2017a. Petrography of four CP-IDPs (abstract #1642). 48th Lunar and Planetary Science Conference. CD-ROM.

Gainsforth Z., Lauretta D. S., Tamura N., Westphal A. J., Jilly-Rehak C. E., and Butterworth A. L. 2017b. Insights into solar nebula formation of pyrrhotite from nanoscale disequilibrium phases produced by H_2S sulfidation of Fe metal. *American Mineralogist* 102:1881–1893.

Giannozzi P., Baroni S., Bonini N., Calandra M., Car R., Cavazzoni C., Ceresoli D., Chiarotti G. L., Cococcioni M., Dabo I., Dal Corso A., De Gironcoli S., Fabris S., Fratesi G., Gebauer R., Gerstmann U., Gougoussis C., Kokalj A., Lazzeri M., Martin-Samos L., Marzari N., Mauri F., Mazzarello R., Paolini S., Pasquarello A., Paulatto L., Sbraccia C., Scandolo S., Sclauzero G., Seitsonen A. P., Smogunov A., Umari P., and Wentzcovitch R. M. 2009. QUANTUM ESPRESSO: A modular and open-source software project for quantum simulations of materials. *Journal of Physics: Condensed Matter* 21:395502.

Hörz F. 2000. Impact features and projectile residues in aerogel exposed on Mir. *Icarus* 147:559–579.

Hörz F., Bastien R., Borg J., Bradley J. P., Bridges J. C., Brownlee D. E., Burchell M. J., Chi M., Cintala M. J., Dai Z. R., Djouadi Z., Dominguez G., Economou T. E., Fairey S. A. J., Floss C., Franchi I. A., Graham G. A., Green S. F., Heck P., Hoppe P., Huth J., Ishii H., Kearsley A. T., Kissel J., Leitner J., Leroux H., Marhas K., Messenger K., Schwandt C. S., See T. H., Snead C., Stadermann I. F. J., Stephan T., Stroud R., Teslich N., Trigo-Rodriguez J. M., Tuzzolino A. J., Troadec D., Tsou P., Warren J., Westphal A. J., Wozniakiewicz P., Wright I., and Zinner E. 2006. Impact features on Stardust: Implications for comet 81P/Wild 2 dust. *Science* 314:1716–1719.

Ishii H. A., Bradley J. P., Dai Z. R., Chi M., Kearsley A. T., Burchell M. J., Browning N. D., and Molster F. 2008. Comparison of Comet 81P/Wild 2 dust with interplanetary dust from comets. *Science* 319:447.

Jain A., Ong S. P., Hautier G., Chen W., Richards W. D., Dacek S., Cholia S., Gunter D., Skinner D., Ceder G., and Persson K. A. 2013. Commentary: The Materials Project: A materials genome approach to accelerating materials innovation. *APL Materials* 1:011002.

Joswiak D. J., Brownlee D. E., and Bradley J. P. 1996. Systematic analyses of major element distributions in GEMS from high speed IDPs. Proceedings, 27th Lunar and Planetary Science Conference. pp. 625–626.

Joswiak D. J., Brownlee D. E., Pepin R. O., and Schlutter D. J. 2005. Densities and mineralogy of cometary and asteroidal interplanetary dust particles collected in the stratosphere. Workshop on Dust in Planetary Systems. pp. 141–144.

Joswiak D. J., Brownlee D. E., Matrajt G., Westphal A. J., and Snead C. J. 2009. Kosmochloric Ca-rich pyroxenes and FeO-rich olivines (Kool grains) and associated phases in Stardust tracks and chondritic porous interplanetary dust particles: Possible precursors to FeO-rich type II chondrules in ordinary chondrites. *Meteoritics & Planetary Science* 44:1561–1588.

Joswiak D. J., Brownlee D. E., Matrajt G., Westphal A. J., Snead C. J., and Gainsforth Z. 2012. Comprehensive examination of large mineral and rock fragments in Stardust tracks: Mineralogy, analogous extraterrestrial materials, and source regions. *Meteoritics & Planetary Science* 47:471.

Joswiak D. J., Brownlee D. E., Nguyen A. N., and Messenger S. 2017. Refractory materials in comet samples. *Meteoritics & Planetary Science* 52:1612–1648.

Keller L. P. and Messenger S. 2005. The nature and origin of interplanetary dust: High-temperature components. *Chondrites and the Protoplanetary Disk* 341:657–667.

Keller L. P., and Messenger S. 2009. Equilibrated aggregates in cometary IDPs: Insights into the crystallization process in protoplanetary disks (abstract #2121). 40th Lunar and Planetary Science Conference. CD-ROM.

Keller L. P., and Messenger S. 2011. On the origins of GEMS grains. *Geochimica et Cosmochimica Acta* 75:5336–5365.

Lauretta D. S. 2005. Sulfidation of an iron–nickel–chromium–cobalt–phosphorus alloy in 1% H_2S–H_2 gas mixtures at 400–1000◦C. *Oxidation of Metals* 64:1–22.

Lejaeghere K., Bihlmayer G., Bjorkman T., Blaha P., Blugel S., Blum V., Caliste D., Castelli I. E., Clark S. J., Dal Corso A., De Gironcoli S., Deutsch T., Dewhurst J. K., Di Marco I., Draxl C., Dułak M., Eriksson O., Flores-Livas J. A., Garrity K. F., Genovese L., Giannozzi P., Giantomassi M., Goedecker S., Gonze X., Granas O., Gross E. K. U., Gulans A., Gygi F., Hamann D. R., Hasnip P. J., Holzwarth N. A. W., Iuşan D., Jochym D. B., Jollet F., Jones D., Kresse G., Koepernik K., Kucukbenli E., Kvashnin Y. O., Locht I. L. M., Lubeck S., Marsman M., Marzari N., Nitzsche U., Nordstrom L., Ozaki T., Paulatto L., Pickard C. J., Poelmans W., Probert M. I. J., Refson K., Richter M., Rignanese G. M., Saha S., Scheffler M., Schlipf M., Schwarz K., Sharma S., Tavazza F., Thunstrom P., Tkatchenko A., Torrent M., Vanderbilt D., Van Setten M. J., Van Speybroeck V., Wills J. M., Yates J. R., Zhang G. X., and Cottenier S. 2016. Reproducibility in density functional theory calculations of solids. *Science* 351:aad3000.

Leroux H. and Jacob D. 2013. Fine-grained material encased in microtracks of Stardust samples. *Meteoritics & Planetary Science* 48:1607–1617.

Leroux H., Rietmeijer F. J. M., Velbel M. A., Brearley A. J., Jacob D., Langenhorst F., Bridges J. C., Zega T. J., Stroud R. M., Cordier P., Harvey R. P., Lee M., Gounelle M., and Zolensky M. E. 2008a. A TEM study of thermally modified comet 81P/Wild 2 dust particles by interactions with the aerogel matrix during the Stardust capture process. *Meteoritics & Planetary Science* 43:97–120.

Leroux H., Stroud R. M., Dai, Z. R., Graham G. A., Troadec D., Bradley J. P., Teslich N., Borg J., Kearsley A. T., and Hörz F. 2008b. Transmission electron microscopy of cometary residues from micron-sized craters in the Stardust Al foils. *Meteoritics & Planetary Science* 43:143–160.

Lodders K. 2003. Solar system abundances and condensation temperatures of the elements. *The Astrophysical Journal* 591:1220–1247.

Love S. G. and Brownlee D. E. 1991. Heating and thermal transformation of micrometeoroids entering the Earth's atmosphere. *Icarus* 89:26–43.

Matrajt G., Ito M., Wirick S., Messenger S., Brownlee D. E., Joswiak D., Flynn G., Sandford S. A., Snead C., and Westphal A. J. 2008. Carbon investigation of two Stardust particles: A TEM, NanoSIMS, and XANES study. *Meteoritics & Planetary Science* 43:315–334.

Messenger S., Nakamura-Messenger K., Keller L. P., and Clemett S. J. 2015. Pristine stratospheric collection of interplanetary dust on an oil-free polyurethane foam substrate. *Meteoritics & Planetary Science* 50:1468–1485.

Nakamura T., Noguchi T., Tsuchiyama A., Ushikubo T., Kita N. T., Valley J. W., Zolensky M. E., Kakazu Y., Sakamoto K., Mashio E., Uesugi K., and Nakano T. 2008. Chondrulelike objects in short-period Comet 81P/Wild 2. *Science* 321:1664–1667.

Noguchi T., Nakamura T., Okudaira K., Yano H., Sugita S., and Burchell M. J. 2007. Thermal alteration of hydrated minerals during hypervelocity capture to silica aerogel at the flyby speed of Stardust. *Meteoritics & Planetary Science* 42:357–372.

Nuth J. A., Hallenbeck S. L., and Rietmeijer F. J. M. 2000. Laboratory studies of silicate smokes: Analog studies of circumstellar materials. *Journal of Geophysical Research* 105:10,387–10,396.

Ogliore R. C., Huss G. R., Nagashima K., Butterworth A. L., Gainsforth Z., Stodolna J., Westphal A. J., Joswiak D., and Tyliszczak T. 2012. Incorporation of a late-forming chondrule into Comet Wild 2. *The Astrophysical Journal* 745:L19.

Ogliore R. C., Nagashima K., Huss G. R., Westphal A. J., Gainsforth Z., and Butterworth A. L. 2015. Oxygen isotopic composition of coarse- and fine-grained material from comet 81P/Wild 2. *Geochimica et Cosmochimica Acta* 166:74–91.

Okudaira K., Noguchi T., Nakamura T., Sugita S., Sekine Y., and Yano H. 2004. Evaluation of mineralogical alteration of micrometeoroid analog materials captured in aerogel. *Advances in Space Research* 34:2299–2304.

Perdew J. P., Burke K., and Ernzerhof M. 1996. Generalized gradient approximation made simple. *Physical Review Letters* 77:3865–3868.

Rietmeijer F. 2009a. A cometary aggregate interplanetary dust particle as an analog for comet Wild 2 grain chemistry preserved in silica-rich Stardust glass. *Meteoritics & Planetary Science* 44:1589–1609.

Rietmeijer F. J. M. 2009b. Chemical identification of comet 81P/Wild 2 dust after interacting with molten silica aerogel. *Meteoritics & Planetary Science* 44:1121–1132.

Rietmeijer F. J. M. 2015. The smallest comet 81P/Wild 2 dust dances around the CI composition. *Meteoritics & Planetary Science* 50:1767–1789.

Rietmeijer F. J. M. and Nuth J. A. I. 2000. Metastable eutectic equilibrium brought down to Earth. *EOS* 81:409–420.

Roskosz M., Leroux H., and Watson H. C. 2008. Thermal history, partial preservation and sampling bias recorded by Stardust cometary grains during their capture. *Earth and Planetary Science Letters* 273:195–202.

Rotundi A., Sierks H., Della Corte V., and Fulle M. 2015. Dust measurements in the coma of comet 67P/Churyumov-Gerasimenko inbound to the Sun. *Science* 347:aaa3905.

Shu F. H. 1992. *The physics of astrophysics: Gas dynamics*. Sausalito, California: University Science Books.

Sierks H., Barbieri C., Lamy P. L., Rodrigo R., Koschny D., Rickman H., Keller H. U., Agarwal J., A'Hearn M. F., Angrilli F., Auger A.-T., Barucci M. A., Bertaux J.-L., Bertini I., Besse S., Bodewits D., Capanna C., Cremonese G., Da Deppo V., Davidsson B., Debei S., De Cecco M., Ferri F., Fornasier S., Fulle M., Gaskell R., Giacomini L., Groussin O., Guitierrez-Marques P., Gutiérrez P. J., Güttler C., Hoekzema N., Hviid S. F., Ip W.-H., Jorda L., Knollenberg J., Kovacs G., Kramm J. R., Kührt E., Küppers M., La Forgia F., Lara L. M., Lazzarin M., Layrat C., Moreno J. J. L., Magrin S., Marchi S., Marzari F., Massironi M., Michalik H., Moissl R., Mottola S., Naletto G., Oklay N., Pajola M., Pertile M., Preusker F., Sabau L., Scholten F., Snodgrass C., Tomas N., Tubiana C., Vincent J.-B., Wenzel K.-P., Zaccariotto M., and Pätzold M. 2015. On the nucleus structure and activity of comet 67P/Churyumov-Gerasimenko. *Science* 347:aaa1044.

Stodolna J., Jacob D., and Leroux H. 2012a. Mineralogy and petrology of Stardust particles encased in the bulb of track 80: TEM investigation of the Wild 2 fine-grained material. *Geochimica et Cosmochimica Acta* 87:35–50.

Stodolna J., Jacob D., Leroux H., and Burchell M. J. 2012b. Microstructure modifications of silicates induced by the collection in aerogel: Experimental approach and comparison with Stardust results. *Meteoritics & Planetary Science* 46:696–707.

Stodolna J., Gainsforth Z., Butterworth A. L., and Westphal A. J. 2014. Characterization of preserved primitive fine-grained material from the Jupiter family comet 81P/Wild 2–A new link between comets and CP-IDPs. *Earth and Planetary Science Letters* 388:367–373.

Tamura N. 2014. XMAS: A versatile tool for analyzing synchrotron X-ray microdiffraction data. In *Strain and dislocation gradients from diffraction spatially-resolved local structure and defects*, edited by Barabash R. and Ice G. London: Imperial College Press. pp. 125–155.

Tamura N., Kunz M., Chen K., Celestre R. S., MacDowell A. A., and Warwick T. 2009. A superbend X-ray microdiffraction beamline at the advanced light source. *Materials Science and Engineering A* 524:28–32.

Trigo-Rodriguez J. M., Dominguez G., Burchell M. J., Hörz F., and Llorca J. 2008. Bulbous tracks arising from hypervelocity capture in aerogel. *Meteoritics & Planetary Science* 43:75–86.

Tsatis D. and Theodossiou A. 1982. Thermal diffusivity in pyrrhotite (Fe_7S_8). *Journal of Physics and Chemistry of Solids* 43:771–772.

Vanderbilt D. 1990. Soft self-consistent pseudopotentials in a generalized eigenvalue formalism. *Physical Review B* 41:7892–7895.

Westphal A. J., Snead C., Butterworth A. L., Graham G. A., Bradley J. P., Bajt S., Grant P. G., Bench G., Brennan S., and Pianetta P. 2004. Aerogel keystones: Extraction of complete hypervelocity impact events from aerogel collectors. *Meteoritics & Planetary Science* 39:1375–1386.

Wooden D. H., Ishii H. A., and Zolensky M. E. 2017. Cometary dust: The diversity of primitive refractory grains. *Philosophical Transactions of the Royal Society A: Mathematical, Physical and Engineering Sciences* 375:20160260.

SUPPORTING INFORMATION

Additional supporting information may be found in the online version of this article.

Fig. S1. A) TEM brightfield image of FGM12. B) EDS map of FGM12 showing Cr-rich spinels dotting the periphery.

Fig. S2. A) HRTEM image of FGM15 with a 20 nm scale bar. B) Combination of 35 digital darkfield images of FGM15 showing that the object is multiphase crystalline throughout.

Fig. S3. A) HRTEM image of a portion of FGM17. B) Digital darkfield reconstructions using chromite d-spacings. Red: 044 reflections, green: 113, blue: 111.

Fig. S4. A) Brightfield TEM image of FGM18 with 100 nm scale bar. B) EDS map with metals and sulfides (red), a weblike structure of Mg (green) and silicate (blue).

Fig. S5. A) HAADF image of FGM20 with 100 nm scale bar after a 12 minute EDS map. The sulfide impactor is to the left. Arrows indicate the location of beam-sensitive Fe-oxides. B) EDS map of the region showing Fe-metal (solid red), Fe-oxide (textured red), magnesium silicate (green) and sulfide (purple).

Table S1. Nanophase compositions of capture modified objects from TEM EDS Normalized to Mg and CI.

Table S2. Sample ID numbers.